

# Cause-and-effect of linear mechanisms sustaining wall turbulence

Adrián Lozano-Durán<sup>1†</sup>, Navid C. Constantinou<sup>2</sup>,  
Marios-Andreas Nikolaidis<sup>3</sup>, and Michael Karp<sup>1</sup>

<sup>1</sup>Center for Turbulence Research, Stanford University, CA 94305, USA

<sup>2</sup>Research School of Earth Sciences and ARC Centre of Excellence for Climate Extremes,  
Australian National University, Canberra ACT 2601, Australia

<sup>3</sup>Department of Physics, National and Kapodistrian University of Athens, Athens 157 72,  
Greece

Despite the nonlinear nature of turbulence, there is evidence that the energy-injection mechanisms sustaining wall turbulence can be ascribed to linear processes. The different scenarios stem from linear stability theory and comprise exponential instabilities from mean-flow inflection points, neutral modes, transient growth from non-normal operators, and parametric instabilities from temporal mean-flow variations, among others. These mechanisms, each potentially capable of leading to the observed turbulence structure, are rooted in simplified theories and conceptual arguments. Whether the flow follows any or a combination of them remains unclear. Here, we devise a collection of numerical experiments in which the Navier–Stokes equations are sensibly modified to quantify the role of the different linear mechanisms at low Reynolds number ( $\text{Re}_\tau \approx 180$ ). We achieve this by direct numerical simulation of turbulent channel flows, in which the energy transfer from the streamwise-averaged mean-flow ( $\mathbf{U}$ ) to the fluctuating velocities ( $\mathbf{u}'$ ) is constrained to preclude a targeted linear mechanism. In contrast to other studies, our approach allows for direct evaluation of cause-and-effect links between the linear energy injection from  $\mathbf{U}$  to  $\mathbf{u}'$  in a fully nonlinear setup. Our results show that turbulence persists when exponential instabilities and neutral modes of the mean flow are suppressed. Removing all exponential instabilities from the flow only leads to a 10% reduction of turbulent velocity fluctuations. We also show that the energy transfer from  $\mathbf{U}$  to  $\mathbf{u}'$  via transient growth alone, without exponential and parametric instabilities, is sufficient for sustaining turbulence. Finally, we demonstrate that a collection of simulations with frozen-in-time  $\mathbf{U}$  exclusively supported by transient growth provides a faithful representation of the actual time-varying energy transfer from  $\mathbf{U}$  to  $\mathbf{u}'$ .

---

## 1. Introduction

Turbulence is a highly nonlinear phenomenon. Nevertheless, there is ample agreement that the energy-injection mechanisms sustaining wall-turbulence can be partially attributed to linear processes (Jiménez 2013). The different mechanisms have their origins in linear stability theory (Reynolds & Hussain 1972; Hamilton *et al.* 1995; Waleffe 1997; Schoppa & Hussain 2002; Del Álamo & Jiménez 2006; Hwang & Cossu 2010, 2011) and constitute the foundations of many control and modelling strategies (Kim & Bewley

† Email address for correspondence: adrianld@stanford.edu

2006; Schmid & Henningson 2012; McKeon 2017; Zare *et al.* 2020). Despite the ubiquity of linear theories, the significance of different instabilities in fully developed turbulence remains outstanding, and its relevance is consequential to comprehend, model, and control the structure of wall-bounded turbulence by linear methods (e.g. Högberg *et al.* 2003; Del Álamo & Jiménez 2006; Hwang & Cossu 2010; Zare *et al.* 2017; Morra *et al.* 2019; Towne *et al.* 2020). Here we evaluate the various energy transfer mechanisms from the mean flow to the fluctuations in wall turbulence. We devise a collection of numerical experiments of turbulent flows over a flat wall, in which the Navier–Stokes equations are minimally altered to suppress the energy transfer from the mean flow to the fluctuating velocities via different linear mechanisms.

Several linear mechanisms have been proposed as plausible scenarios to rationalise the transfer of energy from the large-scale mean flow to the fluctuating velocities. Before diving into the intricacies of each mechanism, one may ask why we should insist on describing this energy transfer using linear theories if turbulence is undoubtedly a nonlinear phenomenon. One reason is that the energy source for turbulent fluctuations in shear flows is controlled by spatial differences across the mean velocity profile, which naturally reduces to a linear model (Brown & Roshko 1974; Jiménez 2013). It has been demonstrated in many occasions that the large scales of turbulent flows in strongly inhomogeneous environments do behave linearly at heart (Schmid 2007). Wall turbulence with large-scale pressure or body forces imposed, e.g., in the streamwise direction is such an example. Also geophysical flows, in which rotation and stratification impose strong constraints on the flow. An additional motivation for the use of linear theories is a matter of practicality: our current framework to analyse linear systems is well beyond the tools to understand nonlinear equations. Hence, inasmuch the linear equations meaningfully represents the physics of the problem, linear tools greatly aid the analysis.

Clarified the convenience of linear theories, the next step is to select a reference base flow to linearise the flow about. It is generally agreed that the ubiquitous streamwise rolls (regions of rotating fluid) and streaks (regions of low and high streamwise velocity with respect to the mean) (Klebanoff *et al.* 1962; Kline *et al.* 1967) are involved in a quasi-periodic regeneration cycle (Panton 2001; Adrian 2007; Smits *et al.* 2011; Jiménez 2012, 2018; Lozano-Durán *et al.* 2019) and that their space-time structure plays a crucial role in sustaining shear-driven turbulence (e.g. Kim *et al.* 1971; Jiménez & Moin 1991; Butler & Farrell 1993; Hamilton *et al.* 1995; Waleffe 1997; Schoppa & Hussain 2002; Farrell & Ioannou 2012; Jiménez 2012; Constantinou *et al.* 2014; Farrell *et al.* 2016; Lozano-Durán *et al.* 2018). Accordingly, the flow is often decomposed into two components: a base flow defined through some averaging procedure over the instantaneous flow, and the three-dimensional fluctuations (or perturbations) about that base flow. In this manner, the ultimate cause maintaining turbulence is conceptualised as the energy transfer from the base flow to the fluctuating flow, as sketched in figure 1.

The decomposition of the base flow–fluctuations stands as the most important decision in the linearisation process, as the physical mechanisms ascribed to the linearised equations depend crucially on this choice. Various base flows have been proposed in the literature depending on the number of spatial directions and time interval to average the flow. For example, a common choice is to average the flow in all homogeneous directions and time (e.g., Reddy & Henningson 1993; Del Álamo & Jiménez 2006; McKeon 2017). Here, we take our base flow  $\mathbf{U}$  to consist of the instantaneous streamwise-averaged velocity  $U(y, z, t)$  in the streamwise ( $x$ ) direction with zero wall-normal ( $V = 0$ ) and spanwise ( $W = 0$ ) flow, where  $y$  and  $z$  are the wall-normal and spanwise directions respectively; see figure 1. Our choice is supported by previous studies (Waleffe 1997; Schoppa & Hussain 2002; Farrell & Ioannou 2012). Yet, there is no obvious *a priori*

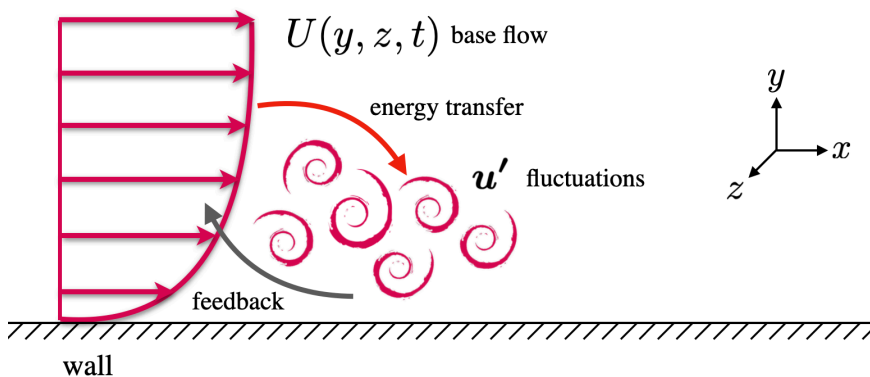


Figure 1: Schematic of the energy transfer from the base flow  $\mathbf{U} = U(y, z, t)\hat{x}$  to the fluctuating velocities  $\mathbf{u}'$ . The energy transfer (red arrow) from  $\mathbf{U}$  to  $\mathbf{u}'$  can be investigated via the linear dynamics of the governing equation of  $\mathbf{u}'$ . The cycle is closed by the nonlinear feedback of  $\mathbf{u}'$  back to  $\mathbf{U}$  (gray arrow).

justification for selecting  $U(y, z, t)$  in favour of other alternatives base flows, and one of the goals here is to investigate whether  $U(y, z, t)$  is a meaningful choice to describe the energy transfer from the large scales to the fluctuating flow.

The self-sustaining nature of wall turbulence has also been investigated from the viewpoint of dynamical-systems theory and the stability of the system – the spatio-temporal structure of turbulence may be thought of as a low-dimensional manifold around which the dynamical system spends a substantial fraction of time (Jiménez 1987). According to the dynamical-systems perspective, the simplest description of turbulence is then given by a collection of fixed points and unstable periodic orbits embedded in a high-dimensional turbulent attractor (Kawahara *et al.* 2012). The first dynamical-system investigations of turbulence in shear flows began with nonlinear equilibrium states, referred to as ‘exact coherent structures’, of Couette flow (Nagata 1990). Since then, there have been multiple descriptions of these states in shear flow such as channels and pipes among others, often involving unstable travelling waves (e.g., Waleffe 2001; Kawahara & Kida 2001; Wedin & Kerswell 2004; Gibson *et al.* 2009; van Veen & Kawahara 2011; Kreilos & Eckhardt 2012; Park & Graham 2015; Hwang *et al.* 2016; Sekimoto & Jiménez 2017). Kawahara & Kida (2001) discovered time-periodic orbits for the incompressible Navier–Stokes equations on plane Couette flow that exhibit a full regeneration cycle comprising the formation and breakdown of streamwise vortices and low-velocity streaks. Hall & Smith (1988, 1991) proposed a theoretical nonlinear framework to describe self-sustaining process and transition in terms of vortex–wave interactions (VWI). In the VWI theory, a single downstream propagating wave interacts with itself to produce a spanwise periodic stress jump which drives a roll. The roll then interacts with a neutrally stable mean streamwise flow to produce a streak. Subsequent developments of the VWI theory include extensions to laminar to turbulent transition (Wang *et al.* 2007) and multiscale motions consistent with the logarithmic layer (Hall 2018). Other descriptions of self-sustaining turbulence include the study by Deguchi & Hall (2015), and the semi-analytical model by Chini *et al.* (2017); the latter devoted to the formation and maintenance of uniform momentum zones and interlaced vortical

fissures. While all these theories could provide a plausible explanation for how turbulence self-sustains, we are still lacking direct evidence regarding whether one or a combination of the above-mentioned mechanisms actually at work in realistic turbulent flows.

In this work we will investigate and quantify the role of several linear mechanisms proposed to explain the energy transfer from the mean to the fluctuating flow. The linear mechanisms we deal here are categorised into: (i) modal instability of the mean streamwise flow, (ii) non-modal transient growth, and (iii) non-modal transient growth assisted by parametric instability of the time-varying base flow.

In mechanism (i), it is hypothesised that the energy is transferred from the mean flow  $U(y, z, t)$  to the fluctuating flow through modal inflectional instability in the form of strong spanwise flow variations (Hamilton *et al.* 1995; Waleffe 1997; Karp & Cohen 2017), corrugated vortex sheets (Kawahara *et al.* 2003), or intense localised patches of low-momentum fluid (Andersson *et al.* 2001; Hack & Moin 2018). Inasmuch as the instantaneous realisations of the streaky flow are strongly inflectional, the flow  $U(y, z, t)$  is invariably unstable at a frozen instant of time (Lozano-Durán *et al.* 2018). These inflectional instabilities are markedly robust and, therefore, their excitation has been proposed to be the mechanism that replenishes the perturbation energy of the turbulent flow (Hamilton *et al.* 1995; Waleffe 1997; Andersson *et al.* 2001; Kawahara *et al.* 2003; Hack & Zaki 2014; Hack & Moin 2018). Consequently, the exponential instability of the streak is thought to be central to the maintenance of wall turbulence. The modal character of the base flow is also central in the vortex-wave interaction theory in which it is postulated that the regeneration cycle is supported by the interaction of a roll with the neutrally stable mean streamwise-flow (Hall & Smith 1988, 1991; Hall 2018).

Mechanism (ii), transient growth, involves the redistribution of fluid near the wall by streamwise vortices leading to the formation of streaks through a combination of the the Orr and lift-up mechanisms (Landahl 1975; Farrell & Ioannou 1993*a*; Butler & Farrell 1993; Kim & Lim 2000; Jiménez 2012). In this case, the base flow, while being exponentially stable, supports the growth of perturbations for a period of time due to the non-normality of the linear operator about that very base flow; a process referred to as non-modal transient growth (e.g. Trefethen *et al.* 1993; Butler & Farrell 1993; Farrell & Ioannou 1996*a*; Del Álamo & Jiménez 2006; Schmid 2007; Cossu *et al.* 2009). Other studies suggest that the generation of streaks is due to the structure-forming properties of the linearised Navier–Stokes operator, independent of any organised vortices (Chernyshenko & Baig 2005), but the non-modal transient growth is still invoked. The transient growth scenario gained even more popularity since the work by Schoppa & Hussain (2002) (see also de Giovanetti *et al.* 2017), who argued that transient growth may be the most relevant mechanism not only for streak formation but also for their eventual breakdown. Schoppa & Hussain (2002) showed that most streaks detected in actual wall-turbulence simulations are indeed exponentially stable for the set of wavenumbers considered. Hence, the loss of stability of the streaks would be better explained by the transient growth of perturbations, that would lead to vorticity sheet formation and nonlinear saturation.

Finally, mechanism (iii) has been advanced in recent years by Farrell, Ioannou and coworkers (Farrell & Ioannou 2012; Farrell *et al.* 2016; Nikolaidis *et al.* 2016; Farrell *et al.* 2017; Brethiem *et al.* 2018). They adopted the perspective of statistical state dynamics (SSD) to develop a tractable theory for the maintenance of wall turbulence. Within the SSD framework, the perturbations are maintained by an essentially time-dependent, parametric instability of the base flow. The concept of “parametric instability” refers here to perturbation growth that is inherently caused by the time-dependence of  $U$ . The self-sustaining mechanism proposed by SSD still relies on the highly non-

normal streamwise roll and streak structure. However, it differs from other mechanisms above in that it requires the time-variations of  $U$  for the growth of perturbations to be supported. Furthermore, it implies that mechanisms based on critical layers and modal growth processes (Hall & Smith 1988; Waleffe 1997; Hall & Smith 1991; McKeon & Sharma 2010) are not responsible for the energy transfer from  $U$  to  $\mathbf{u}'$ , since those mechanisms ignore the intrinsic time-dependence of the base flow.

The scenarios (i), (ii), and (iii), although consistent with the observed turbulence structure (Jiménez 2018), are rooted in simplified theoretical arguments. It remains to establish whether self-sustaining turbulence follows predominantly one of the above-mentioned mechanisms, or a combination of them. In this study, we evaluate the contribution of different linear mechanisms via direct numerical simulation of channel flows with constrained energy extraction from the streamwise-averaged mean-flow. To that end, we modify the Navier–Stokes equations to suppress targeted linear mechanisms, while maintaining a fully nonlinear system. This approach falls within the category of “instantiated” causality, i.e., intrusively perturbing a system (cause) and observing the consequences (effect) (Pearl 2009). In our case, the altering of the system has the benefit of providing a clear cause-and-effect assessment of the importance of each linear mechanism implicated in sustaining the flow. Preliminary versions of this work can be found in Lozano-Durán *et al.* (2018) and Lozano-Durán *et al.* (2020). The present work also provides a complementary viewpoint to the study of self-sustaining wall turbulence by Lozano-Durán *et al.* (2019), who introduced a non-intrusive probabilistic measure of causality based on the Shannon entropy.

The study is organised as follows: § 2 contains the numerical details of the turbulent channel flow simulations. The statistics of interest for wall turbulence are reviewed in § 3. In § 4, we briefly outline the linear theories of self-sustaining wall turbulence and evaluate *a posteriori* their potential relevance for sustaining the flow. We devise a channel flow in which the feedback from  $\mathbf{u}'$  to  $\mathbf{U}$  is blocked in § 5. The investigation of wall turbulence with constrained linear mechanisms is presented in § 6, which is further subdivided into two subsections each devoted to the cause-and-effect of exponential instabilities and transient growth. Finally, we conclude in § 7.

## 2. Numerical experiments of minimal turbulent channel flows

To investigate the role of different linear mechanisms, we perform direct numerical simulations of an incompressible turbulent channel flow driven by a constant mean pressure gradient. Hereafter, the streamwise, wall-normal, and spanwise directions of the channel are denoted by  $x$ ,  $y$ , and  $z$ , respectively, the corresponding flow velocity components by  $u$ ,  $v$ ,  $w$ , and pressure by  $p$ . The density of the fluid is  $\rho$ , the kinematic viscosity of the fluid is  $\nu$ , and the channel height is  $h$ . The wall is located at  $y = 0$ , where no-slip boundary conditions apply, whereas free stress and no penetration conditions are imposed at  $y = h$ . The streamwise and spanwise directions are periodic.

The simulations are characterised by the friction Reynolds number,  $\text{Re}_\tau$ , defined as the ratio of the channel height and the viscous length-scale  $\delta_v = \nu/u_\tau$ , where  $u_\tau$  is the characteristic velocity based on the mean friction at the wall. In the present work, the Reynolds number is  $\text{Re}_\tau = h/\delta_v \approx 180$ . The streamwise, wall-normal, and spanwise sizes of the computational domain are  $L_x^+ \approx 337$ ,  $L_y^+ \approx 186$ , and  $L_z^+ \approx 168$ , respectively, where the superscript  $+$  denotes quantities scaled by  $\nu$  and  $u_\tau$ . Jiménez & Moin (1991) showed that turbulence in such domains contains an elementary flow unit comprised of a single streamwise streak and a pair of staggered quasi-streamwise vortices, that reproduce the dynamics of the flow in larger domains. Hence, the current numerical

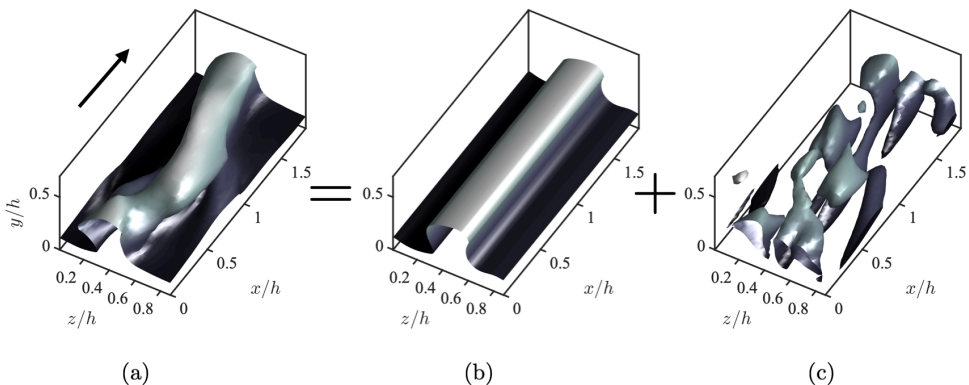


Figure 2: Decomposition of the instantaneous flow into a streamwise mean base flow and fluctuations. Instantaneous isosurface of streamwise velocity for (a) the total flow  $u$ , (b) the streak base flow  $U$ , and (c) the absolute value of the fluctuations  $|u'|$ . The values of the isosurfaces are 0.6 (a and b) and 0.1 (c) of the maximum streamwise velocity. Colours represent the distance to the wall located at  $y = 0$ . The arrow in panel (a) indicates the mean flow direction.

experiment provides a fundamental testbed for studying the self-sustaining cycle of wall turbulence in the buffer layer.

We integrate the incompressible Navier–Stokes equations

$$\frac{\partial \mathbf{u}}{\partial t} = -\mathbf{u} \cdot \nabla \mathbf{u} - \frac{1}{\rho} \nabla p + \nu \nabla^2 \mathbf{u} + \mathbf{f}, \quad (2.1a)$$

$$\nabla \cdot \mathbf{u} = 0, \quad (2.1b)$$

with  $\mathbf{u} \stackrel{\text{def}}{=} (u, v, w)$  and  $\mathbf{f} = (u_\tau^2/h, 0, 0)$ .

Our focus is on the dynamics of the fluctuating velocities  $\mathbf{u}' \stackrel{\text{def}}{=} (u', v', w')$ , defined with respect to the time-varying streak base flow  $\mathbf{U} \stackrel{\text{def}}{=} (U, 0, 0)$ , where

$$U(y, z, t) \stackrel{\text{def}}{=} \langle u \rangle_x = \frac{1}{L_x} \int_0^{L_x} u(x, y, z, t) dx, \quad (2.2)$$

such that  $u' \stackrel{\text{def}}{=} u - U$ ,  $v' \stackrel{\text{def}}{=} v$ , and  $w' \stackrel{\text{def}}{=} w$ . Hereafter,  $\langle \cdot \rangle_{ijk\dots}$  denotes averaging over the directions (or time)  $i, j, k, \dots$ , for example,

$$\langle u \rangle_{xzt} = \frac{1}{L_x L_z T_s} \int_0^{L_x} \int_0^{L_z} \int_0^{T_s} u(x, y, z, t) dt dz dx. \quad (2.3)$$

We have not included contributions from the streamwise averages of  $v$  and  $w$  components in the base flow (2.2), as is traditionally done in the study of stability of the streaky flow (Reddy & Henningson 1993; Waleffe 1997; Schoppa & Hussain 2002). Figure 2 illustrates this flow decomposition while figure 3 depicts three typical snapshots of base flow defined in (2.2).

The equation of motion for the base flow  $\mathbf{U}$  is obtained by averaging the Navier–Stokes



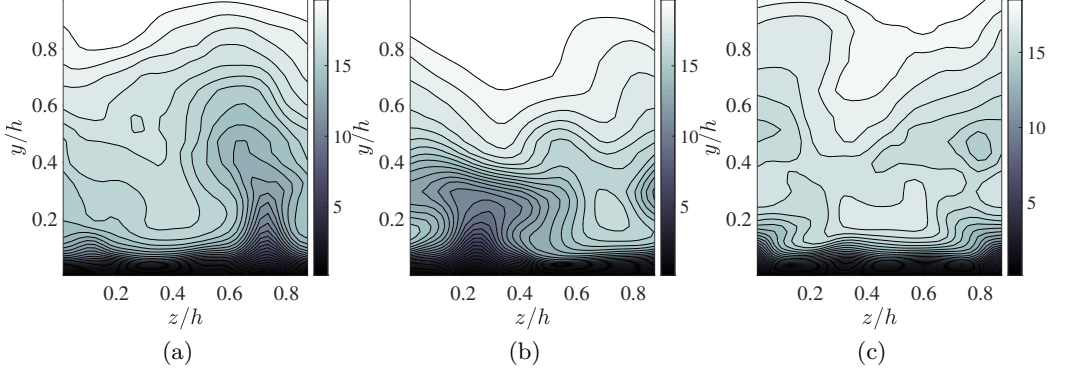


Figure 3: Examples of base flow, defined as  $U(y, z, t) \stackrel{\text{def}}{=} \langle u \rangle_x$ , for a turbulent channel flow at  $\text{Re}_\tau \approx 180$  (case R180 from § 3). The examples are representative of instants of (a,b) strong streak activity (c) and quiescent times.

equations (2.1) in the streamwise direction,

$$\frac{\partial \mathbf{U}}{\partial t} + \mathbf{U} \cdot \nabla \mathbf{U} = -\langle \mathbf{u}' \cdot \nabla \mathbf{u}' \rangle_x - \frac{1}{\rho} \nabla \langle p \rangle_x + \nu \nabla^2 \mathbf{U} + \mathbf{f}, \quad (2.4a)$$

$$\nabla \cdot \mathbf{U} = 0. \quad (2.4b)$$

Subtracting (2.4) from (2.1) we get that the fluctuating flow  $\mathbf{u}'$  is governed by

$$\frac{\partial \mathbf{u}'}{\partial t} = \underbrace{\mathcal{L}(\mathbf{U})\mathbf{u}'}_{\text{linear processes}} + \underbrace{\mathbf{N}(\mathbf{u}')}_{\text{nonlinear processes}}, \quad (2.5)$$

where  $\mathcal{L}(\mathbf{U})$  is the linearised Navier–Stokes operator for the fluctuating state vector about the instantaneous  $\mathbf{U}$  (see figure 2b) such that

$$\mathcal{L}(\mathbf{U})\mathbf{u}' = \mathcal{P} [-\mathbf{U} \cdot \nabla \mathbf{u}' - \mathbf{u}' \cdot \nabla \mathbf{U} + \nu \nabla^2 \mathbf{u}'], \quad (2.6)$$

with  $\mathcal{P}$  the operator that accounts for the kinematic divergence-free condition  $\nabla \cdot \mathbf{u}' = 0$ . Conversely, term  $\mathbf{N}(\mathbf{u}')$  collectively denotes the nonlinear terms, which are quadratic with respect to fluctuating flow fields,

$$\mathbf{N}(\mathbf{u}') \stackrel{\text{def}}{=} \mathcal{P} [-\mathbf{u}' \cdot \nabla \mathbf{u}' + \langle \mathbf{u}' \cdot \nabla \mathbf{u}' \rangle_x]. \quad (2.7)$$

Note that the partition of the right-hand side of (2.5) implies that the energy injection into the velocity fluctuations is ascribed to linear processes from  $\mathcal{L}(\mathbf{U})$ , since the term  $\mathbf{N}(\mathbf{u}')$  is only responsible for redistributing the energy in space and scales among the fluctuations (i.e., the domain-integral of  $\mathbf{u}' \cdot \mathbf{N}$  vanishes).

In the rest of the paper, we will use simulations of the Navier–Stokes equations (2.1) together with modified versions of these equations so that some of the linear mechanisms for energy transfer from the base flow  $\mathbf{U}$  to the fluctuations  $\mathbf{u}'$  are precluded. Table 1 summarises the simulations presented in the paper, highlighting the active linear mechanisms for energy transfer from  $\mathbf{U} \rightarrow \mathbf{u}'$ . The details on how the equations of motion are modified for each case are discussed in the remainder of the paper.

Case	Equation for $\mathbf{u}'$	Equation for $\mathbf{U}$	Feedback from $\mathbf{u}' \rightarrow \mathbf{U}$	Active linear mechanisms for energy transfer from $\mathbf{U} \rightarrow \mathbf{u}'$
R180	(3.1a)	$U(y, z, t)$ from (3.1b)	✓	Exponential instabilities Transient growth Parametric instabilities
NF180	(5.2)	Precomputed $U(y, z, t)$ from R180	✗	Exponential instabilities Transient growth Parametric instabilities
NF-SEI180	(6.1)	Precomputed $U(y, z, t)$ from R180	✗	Transient growth Parametric instabilities
R-SEI180	(6.5a)	$U(y, z, t)$ from (6.5b)	✓	Transient growth Parametric instabilities
NF-TG180	(6.6a)	Precomputed $U(y, z, t_0)$ from R180 at a frozen $t_0$	✗	Transient growth

Table 1: List of cases of turbulent channel flows with and without constrained linear mechanisms. The friction Reynolds number of all the cases is  $\text{Re}_\tau \approx 180$ . The cases are labelled following the nomenclature: R, regular wall turbulence with feedback  $\mathbf{U} \rightarrow \mathbf{u}'$  allowed; NF, no-feedback from  $\mathbf{U} \rightarrow \mathbf{u}'$  allowed; SEI, suppressed exponential instabilities; TG, only transient growth active without exponential nor parametric instabilities.

The simulations are performed with a staggered, second-order, finite differences scheme (Orlandi 2000) and a fractional-step method (Kim & Moin 1985) with a third-order Runge-Kutta time-advancing scheme (Wray 1990). The solution is advanced in time using a constant time step chosen appropriately so that the Courant–Friedrichs–Lewy condition is below 0.5. The code has been presented in previous studies on turbulent channel flows (Lozano-Durán & Bae 2016; Bae et al. 2018, 2019). The streamwise and spanwise resolutions are  $\Delta x^+ \approx 6.5$  and  $\Delta z^+ \approx 3.3$ , respectively, and the minimum and maximum wall-normal resolutions are  $\Delta y_{\min}^+ \approx 0.2$  and  $\Delta y_{\max}^+ \approx 6.1$ . The corresponding grid resolution in  $x$ ,  $y$ , and  $z$  is  $64 \times 90 \times 64$ , respectively. All the simulations presented here were run for at least  $300h/u_\tau$  units of times after transients. The latter time-period is orders of magnitude longer than the typical lifetime of individual energy-containing eddies (Lozano-Durán & Jiménez 2014), which allows us to collect meaningful statistics of the self-sustaining cycle.

### 3. Regular wall turbulence

First, we solve the Navier–Stokes equations without any modification, so that all mechanisms for energy transfers from the base flow to the fluctuations are naturally allowed. We refer to this case as the “regular channel” (R180). We provide an overview of the self-sustaining state of the flow and one-point statistics for R180. The results are used as a reference solution in forthcoming sections. The governing equations for the



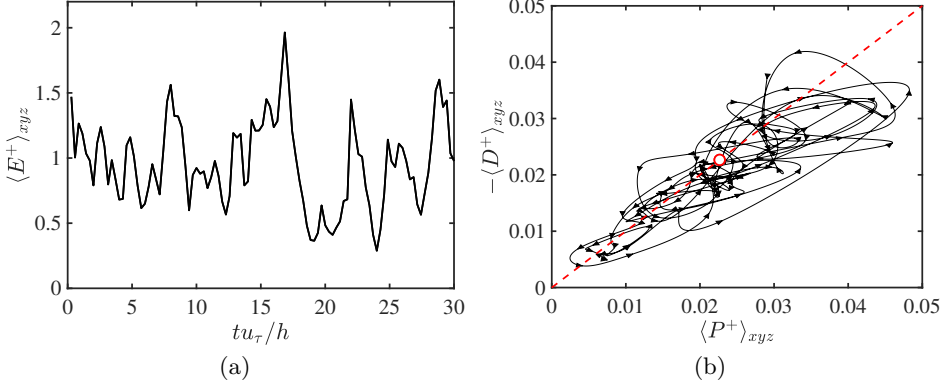


Figure 4: (a) The history of the turbulent kinetic energy of the perturbations  $E = \frac{1}{2}\mathbf{u}' \cdot \mathbf{u}'$  averaged over the channel domain. Note that that only  $30h/u_\tau$  units of time are represented in the panel but the simulation was carried out for more than  $300h/u_\tau$ . (b) Projection of the flow trajectory onto the average production rate  $\langle P \rangle_{xyz}$  and dissipation rate  $\langle D \rangle_{xyz}$  plane. The arrows indicate the time direction of the trajectory, which on average rotates counter-clockwise. The red dashed line is  $\langle P \rangle_{xyz} = -\langle D \rangle_{xyz}$  and the red circle  $\langle P \rangle_{xyz} = -\langle D \rangle_{xyz}$ . The trajectory projected covers  $30h/u_\tau$  units of time. Results for regular channel flow R180.

regular channel flow are (2.4) and (2.5):

$$\frac{\partial \mathbf{u}'}{\partial t} = \mathcal{L}(U)\mathbf{u}' + \mathbf{N}(\mathbf{u}'), \quad (3.1a)$$

$$\frac{\partial U}{\partial t} = -U \cdot \nabla U - \langle \mathbf{u}' \cdot \nabla \mathbf{u}' \rangle_x - \frac{1}{\rho} \nabla \langle p \rangle_x + \nu \nabla^2 U + \mathbf{f}, \quad \nabla \cdot U = 0. \quad (3.1b)$$

The history of the turbulent kinetic energy  $E \stackrel{\text{def}}{=} \frac{1}{2}|\mathbf{u}'|^2$ , is shown figure 4(a) averaged over the full domain,  $\langle E \rangle_{xyz}$ . The evolution of  $\langle E \rangle_{xyz}$  reveals the widely documented intermittent behaviour of the turbulent kinetic energy; relatively low turbulent kinetic energy states follow by occasional spikes usually ascribed to the regeneration and bursting stages of the self-sustaining cycle. An estimate of the bursting period is given by the decorrelation time of  $\langle E \rangle_{xyz}$ , which is  $\sim 5h/u_\tau$  as quantified by the time distance between two consecutive minima in the time-autocorrelation of  $\langle E \rangle_{xyz}$  (not shown). A useful representation of the high dimensional dynamics of the solution is obtained by projecting the instantaneous flow trajectory onto the two-dimensional space defined by the average-in-space production and dissipation rates

$$P \stackrel{\text{def}}{=} -u'v' \frac{\partial U}{\partial y} - u'w' \frac{\partial U}{\partial z}, \quad (3.2)$$

$$D \stackrel{\text{def}}{=} -2\nu \mathcal{S} : \mathcal{S}, \quad (3.3)$$

where  $\mathcal{S}$  is the rate of strain tensor for the fluctuating velocities, and the colon denotes double inner product. The statistically stationary state of the system requires  $\langle P \rangle_{xyzt} = -\langle D \rangle_{xyzt}$ . The results, plotted in figure 4(b), show that the projected solution revolves around  $\langle P \rangle_{xyzt} = -\langle D \rangle_{xyzt}$  and is characterised by excursions into the high dissipation and high production regions consistent with previous works (Jiménez *et al.* 2005). As an example, figure 5 contains the streamwise velocity at three different instants.

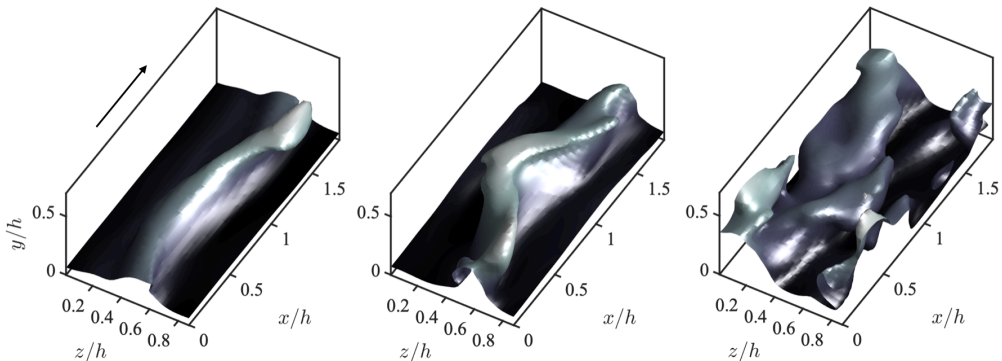


Figure 5: Instantaneous isosurface of the streamwise velocity at different times for R180. The value of the isosurface is 0.65 of the maximum streamwise velocity. Colours represent the distance to the wall located at  $y = 0$ . The arrow indicates the mean flow direction.

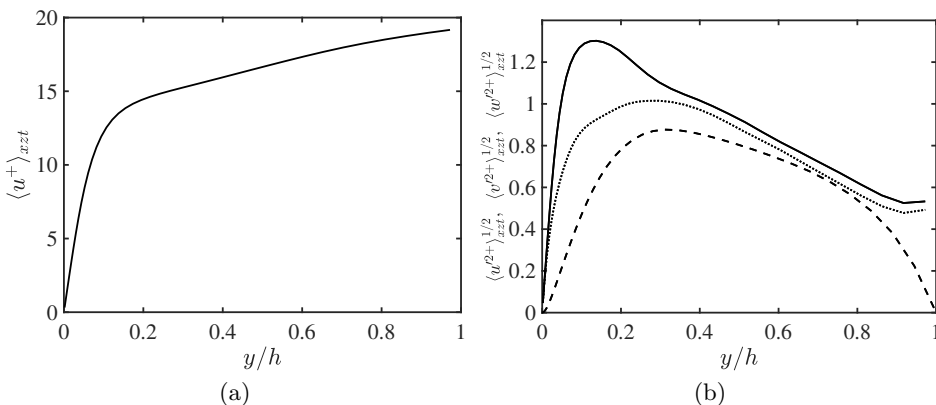


Figure 6: (a) Streamwise mean velocity profile and (b) streamwise (—), wall-normal (---), and spanwise (·····) root-mean-squared fluctuating velocities as a function of the wall-normal distance. Results for regular channel flow R180.

The mean velocity profile and root-mean-squared (rms) fluctuating velocities for the regular channel are shown in figure 6. The results are compiled for the statistical steady state after initial transients. These have also been reported in the literature, with the worth noting difference that here the streamwise fluctuating velocity is defined as  $u' = u - \langle u \rangle_x$ , while in previous studies is common to use instead  $u - \langle u \rangle_{xyzt}$ .

#### 4. Linear theories of self-sustaining wall turbulence: *a posteriori* study

We revisit some linear mechanisms to transfer energy from the base flow to the fluctuating velocities, namely, modal exponential instability and non-modal transient growth. Our focus is on the linear component of (2.5),

$$\frac{\partial \mathbf{u}'_{\text{linear}}}{\partial t} = \mathcal{L}(U) \mathbf{u}'_{\text{linear}}. \quad (4.1)$$

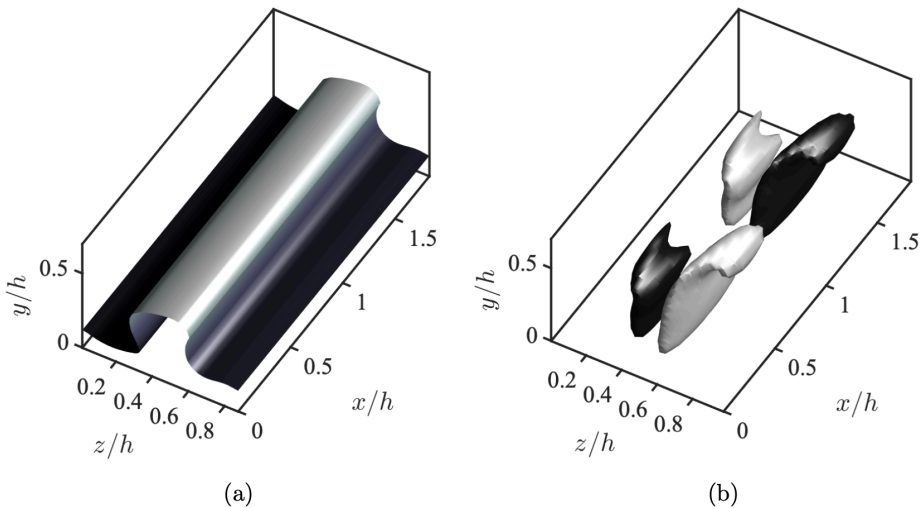


Figure 7: Representative exponential instability of the streak. (a) Instantaneous isosurface of the base flow  $U$ . The value of the isosurface is 0.6 of the maximum and the colour represents the distance to the wall. (b) Isosurface of the instantaneous streamwise velocity for the eigenmode associated with the most unstable eigenvalue  $\lambda_{\max} h/u_\tau \approx 3$  at  $t = 5.1h/u_\tau$ . The values of the isosurface are  $-0.5$  (dark) and  $0.5$  (light) of the maximum streamwise velocity.

The plausibility of each mechanism in  $\mathcal{L}(U)$  as a contender to transfer energy from  $\mathbf{U}$  to  $\mathbf{u}'$  is investigated in a non-intrusive manner by interrogating the data from R180.

#### 4.1. Energy transfer via exponential instability

The first mechanism considered is modal instability of the instantaneous streamwise mean flow. At a given time, the exponential instabilities are obtained by eigen-decomposition of the matrix representation of the linear operator  $\mathcal{L}(U)$  in (2.5),

$$\mathcal{L}(U) = \mathcal{Q}\mathcal{A}\mathcal{Q}^{-1}, \quad (4.2)$$

where  $\mathcal{Q}$  consists of the eigenvectors organised in columns and  $\mathcal{A}$  is the diagonal matrix of associated eigenvalues,  $\lambda_j + i\omega_j$ , with  $\lambda_j, \omega_j \in \mathbb{R}$ .  $\mathcal{Q}^{-1}$  denotes the inverse of  $\mathcal{Q}$ . The base flow is unstable when any of the growth rates  $\lambda_j$  is positive. We provide the details of the stability analysis in Appendix A along with the validation of the calculation in Appendix B. Figure 7 shows a representative example of the streamwise velocity for an unstable eigenmode. The predominant eigenmode has a typical sinuous structure of positive and negative patches of velocity flanking the velocity streak side by side, which may lead to its subsequent meandering and eventual breakdown.

Figure 8(a) shows the probability density functions of the growth rate of the four least stable eigenvalues of  $\mathcal{L}(U)$ . On average, the operator  $\mathcal{L}(U)$  contains 2 to 3 unstable eigenmodes at any given instant. Denoting the Fourier streamwise wavenumber as  $k_x$ , the most unstable eigenmode usually corresponds to  $k_x = 2\pi/L_x$ , although occasionally modes with  $k_x = 2\pi/(2L_x)$  become the most unstable. The history of the maximum growth rate supported by  $\mathcal{L}(U)$ , denoted by  $\lambda_1 = \lambda_{\max}$ , is shown in figure 8(b). The flow is exponentially unstable ( $\lambda_{\max} > 0$ ) more than 90% of the time.

We expect the linear instability to manifest in the flow only when  $\lambda_{\max}$  is much larger

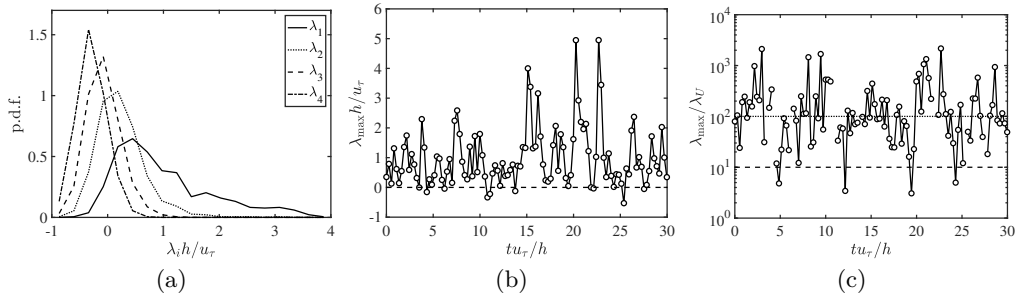


Figure 8: (a) Probability density functions of the growth rate of the four least stable eigenvalues of  $\mathcal{L}(U)$ ,  $\lambda_1 > \lambda_2 > \lambda_3 > \lambda_4$ . (b) The time-series of the most unstable eigenvalue  $\lambda_{\max} = \lambda_1$  of  $\mathcal{L}(U)$ . (c) The time-series of the ratio of  $\lambda_{\max}/\lambda_U$ , where  $\lambda_U$  is the growth rate of the base flow. The horizontal dashed and dotted lines are  $\lambda_{\max}/\lambda_U = 10$  and  $\lambda_{\max}/\lambda_U = 100$ , respectively. Results for regular channel R180.

than time rate of change of the base flow  $U$ , defined as

$$\lambda_U \stackrel{\text{def}}{=} \frac{1}{2} \frac{|\mathrm{d}\langle E_U \rangle_{yz}/\mathrm{d}t|}{\langle E_U \rangle_{yz}}, \quad (4.3)$$

where  $E_U \stackrel{\text{def}}{=} \frac{1}{2} U^2$  is the energy of the base flow (the streak energy). The ratio  $\lambda_{\max}/\lambda_U$  for  $\lambda_{\max} > 0$ , shown in figure 8(c), is about 300 on average, i.e., the time-changes of the streak  $U$  are hundred times slower than the maximum growth rate predicted by the linear stability analysis. Hence, the exponential growth of disturbances is supported for a non-negligible fraction of the flow history, and modal instabilities of  $\mathcal{L}(U)$  stand as a potential mechanism sustaining the fluctuations in wall turbulence. Note that the argument above does not imply that exponential instabilities are necessarily relevant for the flow, but only that they could be realisable in terms of characteristic time-scales.

#### 4.2. Energy transfer via transient growth

The second linear mechanism considered is the non-modal transient growth of the fluctuating flow. The expected scenario of wall turbulence supported by transient growth is the non-modal amplification of  $\mathbf{u}'$  induced by the base flow  $U$  and saturation of  $\mathbf{u}'$ , followed by nonlinear scattering and generation of new disturbances by  $\mathbf{N}$ . The fluctuating flow obeying the linear dynamics of (4.1) can be formally written as:

$$\mathbf{u}'_{\text{linear}}(t+T) = \Phi_{t \rightarrow t+T} \mathbf{u}'_{\text{linear}}(t). \quad (4.4)$$

The propagator  $\Phi_{t \rightarrow t+T}$  maps the fluctuating flow from time  $t$  to time  $t+T$  and represents the cumulative effect of the linear operator  $\mathcal{L}(U)$  during the period from  $t$  to  $t+T$ . If the base flow remains constant for  $t \in [t_0, t_0+T]$ , then we can denote  $\mathcal{L}(U(y, z, t_0)) \mapsto \mathcal{L}_0$  and the propagator simplifies to

$$\Phi_{t_0 \rightarrow t_0+T} = \exp(\mathcal{L}_0 T). \quad (4.5)$$

The exponential growth of the fluctuating velocities was quantified in § 4.1. Here, we are concerned with the transient algebraic growth of  $\mathbf{u}'$  due to the non-normality the linear operator about a frozen base flow,  $\mathcal{L}_0$ . To exclude from the analysis any growth of fluctuations due to the modal instabilities of  $\mathcal{L}_0$ , we consider the modified operator  $\tilde{\mathcal{L}}_0$ ,

$$\tilde{\mathcal{L}}_0 \stackrel{\text{def}}{=} \mathcal{Q} \tilde{\mathcal{A}} \mathcal{Q}^{-1}, \quad (4.6)$$

where  $\tilde{\Lambda}$  is the stabilised version of  $\Lambda$  in (4.2) obtained by setting the real part ( $\lambda_j$ ) of all unstable eigenvalues of  $\Lambda$  equal to  $-\lambda_j$ , while their phase speed and eigenmode structure are left unchanged. (A similar experiment was done by [Farrell & Ioannou \(2012\)](#) for Couette flow at low Reynolds numbers.) It was assessed that the transient growth properties of  $\tilde{\mathcal{L}}_0$  are mostly insensitive to the amount of stabilisation introduced in  $\Lambda$  when  $\lambda_j > 0$  are replaced by  $-a\lambda_j$  with  $a \in [1/4, 4]$ . The potential effectiveness of transient growth due to a base flow  $U(y, z, t_0)$  is then characterised by the energy gain  $G$  over some time-period  $T$ , defined as

$$G(t_0, T, \mathbf{u}'_0) \stackrel{\text{def}}{=} \frac{\langle \mathbf{u}'_T \cdot \mathbf{u}'_T \rangle_{xyz}}{\langle \mathbf{u}'_0 \cdot \mathbf{u}'_0 \rangle_{xyz}} \quad (4.7)$$

where  $\mathbf{u}'_T \stackrel{\text{def}}{=} \mathbf{u}'_{\text{linear}}(x, y, z, t_0 + T)$ ,  $\mathbf{u}'_0 \stackrel{\text{def}}{=} \mathbf{u}'_{\text{linear}}(x, y, z, t_0)$  and  $T$  is the time-horizon for which the gain  $G$  is computed.

The energy, being a bilinear form, can be written in terms of an inner product, e.g.,

$$(\mathbf{u}', \mathbf{u}') \stackrel{\text{def}}{=} \langle \mathbf{u}' \cdot \mathbf{u}' \rangle_{xyz}. \quad (4.8)$$

Using the definition (4.8) and the form of the propagator (4.5) for the frozen linear operator  $\tilde{\mathcal{L}}_0$ , the energy gain is rewritten as:

$$G(t_0, T, \mathbf{u}'_0) = \frac{(\mathbf{u}'_T, \mathbf{u}'_T)}{(\mathbf{u}'_0, \mathbf{u}'_0)} = \frac{(e^{\tilde{\mathcal{L}}_0 T} \mathbf{u}'_0, e^{\tilde{\mathcal{L}}_0 T} \mathbf{u}'_0)}{(\mathbf{u}'_0, \mathbf{u}'_0)} = \frac{(\mathbf{u}'_0, e^{\tilde{\mathcal{L}}_0^\dagger T} e^{\tilde{\mathcal{L}}_0 T} \mathbf{u}'_0)}{(\mathbf{u}'_0, \mathbf{u}'_0)}. \quad (4.9)$$

In the last equality, dagger  $\dagger$  denotes the adjoint operator. Note that, for  $T \rightarrow \infty$ , the growth rate (4.9) tends to 0, since the operator  $\tilde{\mathcal{L}}_0$  is exponentially stable. The maximum gain,  $G_{\max}(t_0, T) = \sup_{\mathbf{u}'_0} (G)$ , is given by the square of the largest singular value of the stabilised linear propagator  $\tilde{\Phi}$  ([Butler & Farrell 1993](#); [Farrell & Ioannou 1996a](#)),

$$\tilde{\Phi}_{t_0 \rightarrow t_0 + T} = \exp(\tilde{\mathcal{L}}_0 T) = \mathcal{M} \Sigma \mathcal{N}^\dagger, \quad (4.10)$$

where  $\Sigma$  is a diagonal matrix, whose positive entries  $\sigma_j$  are the singular values of  $\exp(\tilde{\mathcal{L}}_0 T)$  and the columns of  $\mathcal{M}$  and of  $\mathcal{N}$  are the output modes (or left-singular vectors) and input modes (or right-singular vectors) of  $\exp(\tilde{\mathcal{L}}_0 T)$ , respectively.

The maximum gain  $G_{\max}$  for R180 is shown in figure 9(a) as a function of the optimisation time  $T$ . The values of  $G_{\max}$  also depend on  $t_0$ ; figure 9(a) features the mean and the standard deviation of  $G_{\max}$  for more than 1000 uncorrelated instants  $t_0$ . Figure 9(a) reveals that non-normality alone is potentially able to produce fluctuation energy growth of the order of  $G_{\max} \approx 100$ . On average, the time-horizon for maximum gain is at  $T_{\max} \approx 0.35h/u_\tau$ , by which the auto-correlation of the base flow,

$$\left\langle [U(y, z, t) - \langle U \rangle_t] [U(y, z, t + T) - \langle U \rangle_t] \right\rangle_{xyzt}, \quad (4.11)$$

is around 0.6. The p.d.f. of  $G_{\max}$  at  $T_{\max}$  is shown in figure 9(b) and shows that  $U(y, z, t_0)$  at certain times can support gains as high as 300.

The results here support the hypothesis of transient growth of the “frozen” mean streamwise flow  $U(y, z, t_0)$  as a tenable candidate to sustain wall turbulence. It is worth noting that the maximum gain  $G_{\max}$  provided by the streak base flow  $U(y, z, t_0)$  is considerably larger than the limited gains of around 10 reported in previous studies focused in the buffer layer ([Del Álamo & Jiménez 2006](#); [Pujals \*et al.\* 2009](#); [Cossu \*et al.\* 2009](#)). In the latter works, the base flow selected was  $\langle u \rangle_{xzt}$ , which lacks any spanwise  $z$ -structure and, hence supports lower gains compared to  $U$ .

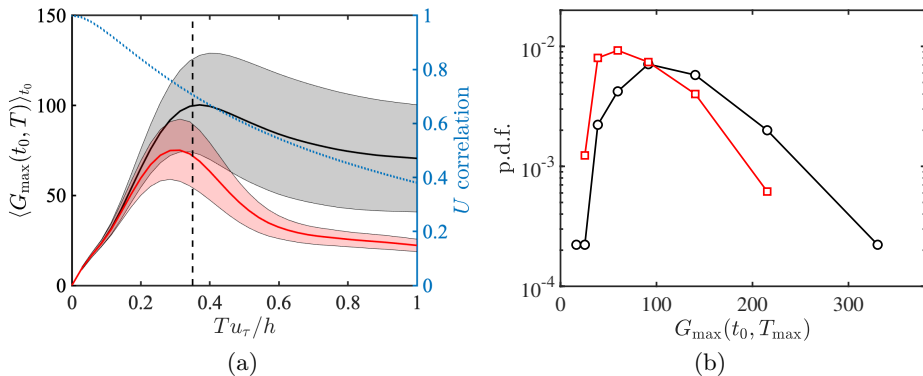


Figure 9: (a) Solid lines are the ensemble mean maximum energy gains  $G_{\max}$  that is supported by  $\tilde{\mathcal{L}}$  over different initial instances  $t_0$ , as a function of the time horizon  $T$ . Shaded regions represents  $\pm$  half standard deviation of  $G_{\max}(t_0, T)$  for a given  $T$ . Black colour shows  $G_{\max}$  for a frozen base flow,  $\tilde{\Phi}_{t_0 \rightarrow t_0+T} = \exp[\tilde{\mathcal{L}}(U(y, z, t_0))T]$ , and red colour for time-varying base flow,  $\tilde{\Phi}_{t_0 \rightarrow t_0+T}^t = \exp[\int_{t_0}^{t_0+T} \tilde{\mathcal{L}}(U(y, z, t)) dt]$ . The vertical dashed line denotes  $T_{\max} = 0.35h/u_\tau$ . The blue dotted line is the auto-correlation of the base flow and its values appear on the right vertical axis. (b) Probability density function of  $G_{\max}(t_0, T_{\max})$ , (—,  $\tilde{\Phi}_{t_0 \rightarrow t_0+T}$ ) time-varying base flow (—,  $\tilde{\Phi}_{t_0 \rightarrow t_0+T}^t$ ). Results for regular channel R180.

As an example, figure 10 provides a visual representation of the input and output modes associated with the maximum optimal gain for one selected instant  $t_0$ . The flow displays a backwards-leaning perturbation (input mode) that is being tilted forward by the mean shear over the time  $T$  (output mode). The process is reminiscent of the linear Orr/lift-up mechanism driven by continuity and wall-normal transport of momentum characteristic of the bursting process and streak formation (Orr 1907; Ellingsen & Palm 1975; Kim & Lim 2000; Jiménez 2013). Unlike other studies that usually take as base flow  $\langle u \rangle_{xyzt}$ , our choice to use  $\langle u \rangle_{xy}$  as base flow limits the spanwise extent of the input and output modes by the  $z$  location of the streak.

#### 4.3. Energy transfer via transient growth with time-varying base flow

In the previous section, we have focused on constant-in-time base flows. We now relax the frozen-base-flow assumption and allow  $U$  to vary in time such that

$$\tilde{\Phi}_{t_0 \rightarrow t_0+T}^t = \exp \left[ \int_{t_0}^{t_0+T} \tilde{\mathcal{L}}(U(y, z, t)) dt \right], \quad (4.12)$$

The propagator  $\tilde{\Phi}_{t_0 \rightarrow t_0+T}^t$  (now with superscript  $t$ ) represents the cumulative effect of  $U(y, z, t)$  from  $t_0$  to  $t_0 + T$ . The gain is given by (Farrell & Ioannou 1996b)

$$G(t_0, T, \mathbf{u}'_0) = \frac{\left( \mathbf{u}'_0, \exp \left( \int_{t_0}^{t_0+T} \tilde{\mathcal{L}}^\dagger dt \right) \exp \left( \int_{t_0}^{t_0+T} \tilde{\mathcal{L}} dt \right) \mathbf{u}'_0 \right)}{(\mathbf{u}'_0, \mathbf{u}'_0)}. \quad (4.13)$$

In contrast with the frozen-flow propagator  $\tilde{\Phi}_{t_0 \rightarrow t_0+T}$  in (4.9), the time variations of the linear operator  $\tilde{\mathcal{L}}(U)$  can either weaken or enhance the energy transfer from  $\mathbf{U}$  to  $\mathbf{u}'$ . Additionally, the gain in (4.13) now admits finite value at  $T \rightarrow \infty$ , despite that  $\tilde{\mathcal{L}}(U)$  is

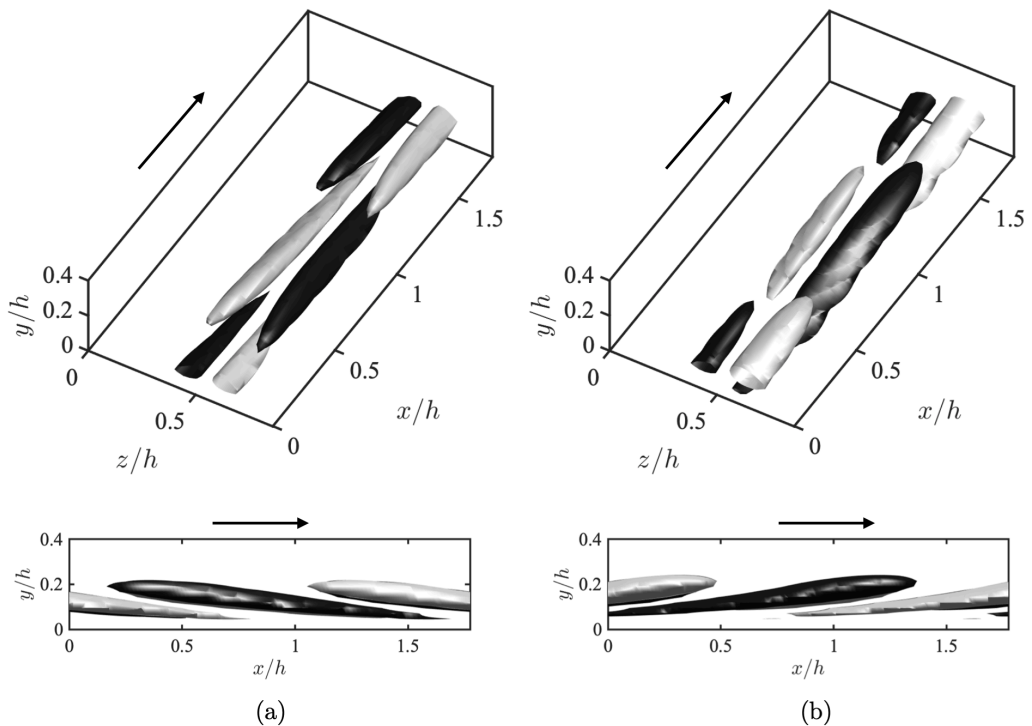


Figure 10: Representative input and output modes associated with transient growth of the streak. Isosurfaces of (a) the input and (b) the output wall-normal velocity mode associated with the largest singular value of  $\tilde{\Phi}_{t_0 \rightarrow t_0+T}$  from (4.9) at  $T = 0.35h/u_\tau$ . The isosurface are  $-0.5$  (dark) and  $0.5$  (light) of the maximum wall-normal velocity. The gain is  $G_{\max} = 136$ . The result is for the regular channel R180.

modally stable. One potential route to achieve finite gain for long times is the parametric instability of the streak discussed in the introduction (Farrell & Ioannou 2012).

To evaluate the algebraic growth with time-varying base flow, we reconstruct the propagator without exponential instabilities  $\tilde{\Phi}_{t_0 \rightarrow t_0+T}^t$  for case R180. To do so, we saved the time-history of  $U(y, z, t)$  from R180 at all time steps and used it to compute  $\tilde{\Phi}_{t_0 \rightarrow t_0+T}^t$  via (4.12). The maximum gain supported by  $\tilde{\Phi}_{t_0 \rightarrow t_0+T}^t$  is compared with its frozen-base-flow counterpart  $\tilde{\Phi}_{t_0 \rightarrow t_0+T}$  in figure 9. The results reveal that energy growth with a time-varying base flow is depleted compared to that of a frozen base flow, suggesting that parametric instabilities might not be an essential ingredient for self-sustaining turbulence. Although not shown for brevity, the input and output modes for the time-varying base flow are again a backwards-leaning perturbation (input mode) that is being tilted forward by the mean shear (output mode), similar to the example shown in figure 10.

## 5. Wall turbulence without explicit feedback from $\mathbf{u}'$ to $\mathbf{U}$

In previous sections, we have acted as if

$$\frac{\partial \mathbf{u}'}{\partial t} = \mathcal{L}(\mathbf{U})\mathbf{u}' + \mathbf{N}(\mathbf{u}'), \quad (5.1)$$



is linear in the term  $\mathcal{L}(U)\mathbf{u}'$ . This is obviously not true because  $U(y, z, t)$  depends on  $\mathbf{u}'$  via the nonlinear feedback term  $-\langle \mathbf{u}' \cdot \nabla \mathbf{u}' \rangle_x$  (see the base-flow evolution equation (3.1b)).

Prior to investigating the cause-and-effect links of linear mechanisms in  $\mathcal{L}(U)$ , we derive a surrogate system in which the energy injection is strictly linear by preventing the explicit feedback from  $\mathbf{u}'$  to  $\mathbf{U}$ . To achieve this, we proceed as follows:

(i) We perform a simulation of R180 for  $600h/u_\tau$  units of time with a constant time step.

(ii) We store the base flow at all time steps. We denote the time-series of this base flow as  $U_0 = U(y, z, t)$  from case R180.

(iii) We time-march the system

$$\frac{\partial \mathbf{u}'}{\partial t} = \mathcal{L}(U_0)\mathbf{u}' + \mathbf{N}(\mathbf{u}'), \quad (5.2)$$

$$U_0 = U(y, z, t) \text{ from case R180.} \quad (5.3)$$

Equation (5.2) is initialised from a random, incompressible velocity field and it is integrated for  $600h/u_\tau$  units of time using the time step as in R180. Equation (5.2) is akin to the Navier–Stokes equations, in which the equation of motion of  $\mathbf{U}$  is replaced by  $\mathbf{U} = (U_0, 0, 0)$ . We refer to this case as “channel flow with no-feedback” or NF180 for short. Note that the base flow  $U_0$  has no *explicit* feedback from  $\mathbf{u}'$  in (5.2), although it has been *implicitly* ‘shaped’ by the velocity fluctuations of R180 and, as such, it contains dynamic information of actual wall turbulence. Hence, the term  $\mathcal{L}(U_0)\mathbf{u}'$  in (5.2) is strictly linear. Also note that  $\mathcal{L}(U_0)$  preserves the modal and non-modal properties of  $\mathcal{L}(U)$  in R180. The flow sustained in NF180 is turbulent as seen in the history of the turbulent kinetic energy in figure 11. Moreover, the footprint of the flow trajectory projected onto the  $\langle P \rangle_{xyz} - \langle D \rangle_{xyz}$  plane also exhibits a similar behaviour to R180 (figure 4b): the flow is organised around  $\langle P \rangle_{xyz} = \langle D \rangle_{xyz}$  with excursions into the high/low dissipation and production regions with predominantly counter-clockwise motions.

The mean turbulence intensities for NF180 are shown in figure 12. Statistics are collected once the system reaches the statistically steady state. The mean velocity profile is omitted as it is identical to that of R180 in figure 6(a). For comparison, figure 12 includes one-point statistics for R180 (previously shown in figure 6(b)). The main consequence of precluding the non-linear feedback from  $\mathbf{u}'$  to  $\mathbf{U}$  is an increase of the level of the turbulence intensities, i.e., the feedback mechanism counteracts the growth of fluctuating velocities in R180. Despite these differences, we can still argue that the turbulence intensities in NF180 are alike those in R180 by noting that the friction velocity  $u_\tau$  is not now the appropriate scaling velocity for NF180. The traditional argument for  $u_\tau$  as the relevant velocity-scale of energy-containing eddies is that the turbulence intensities equilibrate to comply with the mean integrated momentum balance,

$$-\langle uv \rangle \approx u_\tau^2(1 - y/h), \quad (5.4)$$

after viscous effects are neglected (Townsend 1976; Tuerke & Jiménez 2013). As a result,  $u_\tau \approx \sqrt{-\langle uv \rangle / (1 - y/h)}$  stands as the characteristic velocity for all wall-normal distances. A more general argument can be made (Lozano-Durán & Bae 2019) by which the characteristic velocity of the energy-containing eddies,  $u_\star$ , is controlled by the mean production rate of turbulent kinetic energy,  $P \sim u_\star^2/t_\star$ , where  $t_\star$  is the time-scale to extract energy from the mean shear

$$t_\star \sim \frac{1}{\sqrt{(\partial U / \partial y)^2 + (\partial U / \partial z)^2}}. \quad (5.5)$$

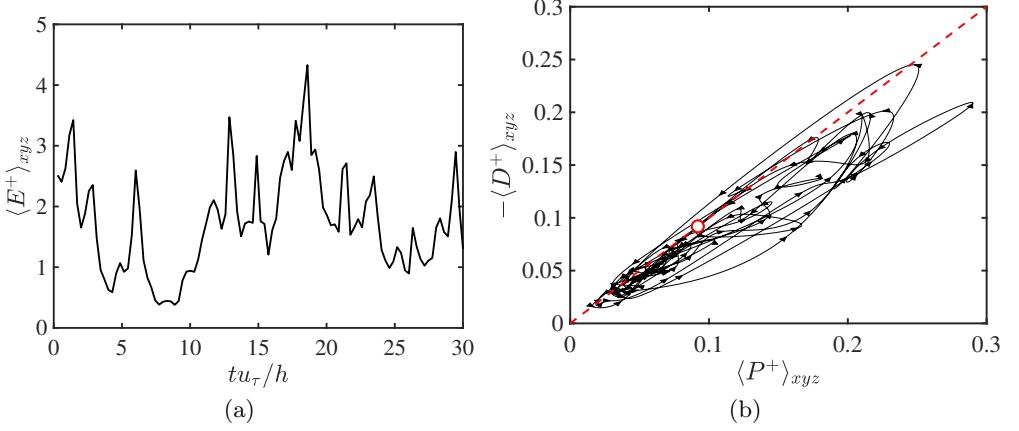


Figure 11: (a) The history of the turbulent kinetic energy of the fluctuations  $E = \frac{1}{2} \mathbf{u}' \cdot \mathbf{u}'$  averaged over the channel domain. Note that that only  $30h/u_\tau$  units of time are shown in the panel but the simulation was carried out for  $600h/u_\tau$ . (b) Projection of the flow trajectory onto the average production rate  $\langle P \rangle_{xyz}$  and dissipation rate  $\langle D \rangle_{xyz}$  plane. The arrows indicate the time direction of the trajectory, which on average rotates counter-clockwise. The red dashed line is  $\langle P \rangle_{xyz} = -\langle D \rangle_{xyz}$  and the red circle  $\langle P \rangle_{xyz} = -\langle D \rangle_{xyz}$ . The trajectory projected covers  $30h/u_\tau$  units of time. The results are for NF180.

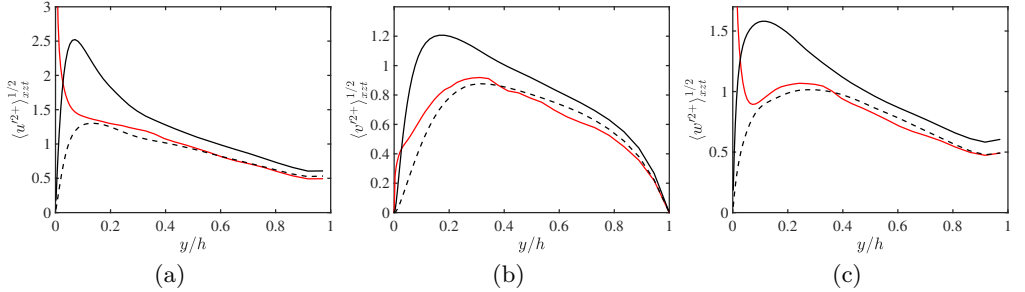


Figure 12: (a) Streamwise, (b) wall-normal, and (c) spanwise mean root-mean-squared fluctuating velocities as a function of the wall-normal distance for case R180 normalised by  $u_\tau$  (---), case NF180 normalised by  $u_\tau$  (—), and NF180 normalised by  $u_\star$  (—).

Then, a characteristic velocity-scale can be constructed as

$$u_\star(y) \stackrel{\text{def}}{=} \left\langle 2\sqrt{\frac{\langle Pt_\star \rangle_{xz}}{1 - y/h}} \right\rangle_t, \quad (5.6)$$

which generalises the concept of friction velocity. The factor  $2/\sqrt{1 - y/h}$  is introduced for convenience in analogy with  $u_\tau$  in (5.4) such that  $u_\star$  reduces to  $\approx u_\tau$  for the regular wall turbulence.

Figure 12 shows that the turbulence intensities, when scaled with  $u_\star$ , resemble those of R180, at least for  $y > 0.1h$  where viscous effects are negligible. This suggests that

the underlying flow dynamics of NF180 is of similar nature as the regular channel case, R180. Thus, hereafter we utilise NF180 as reference case for comparisons.

## 6. Wall turbulence with constrained linear mechanisms

The analysis in §4 is performed *a posteriori* by interrogating the data from R180 in a non-intrusive manner. This provides a valuable insight about the energy injection into the fluctuations but hinders our ability to faithfully assess cause-and-effect links between linear mechanisms and their actual impact on the fully nonlinear system. Here, we follow an intrusive, approach which has the advantage of providing a direct cause-and-effect evaluation of the role played by different linear mechanisms on the energy transfer from the base flow  $\mathbf{U}$  to the fluctuations  $\mathbf{u}'$ . The starting point is the NF180 system of (5.2), in which  $\mathcal{L}(U_0)$  is sensibly modified to suppress a targeted linear mechanism.

### 6.1. Wall turbulence without exponential instability of the streaks

We modify the operator  $\mathcal{L}(U_0)$  so that all the unstable eigenmodes are rendered stable at all times. We refer to this case as the “non-feedback channel with suppressed exponential instabilities” (NF-SEI180) and we inquire whether turbulence is sustained under those conditions. The approach is implemented by replacing  $\mathcal{L}(U_0)$  at each time-instance by the exponentially-stable operator  $\tilde{\mathcal{L}}(U_0)$ , introduced in (4.6). The governing equations for the channel with suppressed exponential instabilities are

$$\frac{\partial \mathbf{u}'}{\partial t} = \tilde{\mathcal{L}}(U_0) \mathbf{u}' + \mathbf{N}(\mathbf{u}'), \quad (6.1)$$

$$U_0 = U(y, z, t) \text{ from case R180.} \quad (6.2)$$

The stable counterpart of  $\mathcal{L}(U_0)$  given by  $\tilde{\mathcal{L}}(U_0)$  guarantees an exponentially stable wall turbulence with respect to the base flow at all times, while leaving other linear mechanisms almost intact. Note that the analysis §4.1 was performed *a posteriori* using data from R180, while in the present case the nonlinear dynamical system (6.1) is actually integrated in time. The simulation was initialised using a flow field from R180, from which the unstable and neutral modes are projected out, and then integrated in time for  $300h/u_\tau$  after transients.

It is useful to note that the modification in (6.1) can be interpreted in terms of a linear forcing if we consider the approximation to  $\tilde{\mathcal{L}}(U_0)$  given by

$$\hat{\mathcal{L}}(U_0) = \mathcal{L}(U_0) - \sum_{j=1}^n 2\lambda_j \mathbf{u}_j \mathbf{u}_j^\dagger \approx \tilde{\mathcal{L}}(U_0), \quad (6.3)$$

where  $\mathbf{u}_j$  is the eigenmode of  $\mathcal{L}(U_0)$  associated with eigenvalue  $\lambda_j > 0$ , and  $n$  is the total number of unstable eigenvalues. Equation (6.3) is approximate, as  $\mathcal{L}(U_0)$  is highly non-normal. However, we confirmed that the eigenvalues of  $\hat{\mathcal{L}}(U_0)$  and  $\tilde{\mathcal{L}}(U_0)$  are almost equal most of the time (Appendix C). In virtue of (6.3), the modification of  $\mathcal{L}(U_0)$  in (6.3) is easily interpretable: stabilising  $\mathcal{L}(U_0)$  is equivalent to introducing a linear drag term,  $-\mathcal{F}\mathbf{u}'$  with

$$\mathcal{F} = \sum_{j=1}^n 2\lambda_j \mathbf{u}_j \mathbf{u}_j^\dagger, \quad (6.4)$$

that counteracts the growth of the unstable modes at a rate proportional of the growth rate of the mode itself.

The results of integrating (6.1) are presented in figure 13 and 14. The p.d.f.s of  $\lambda_j$  and

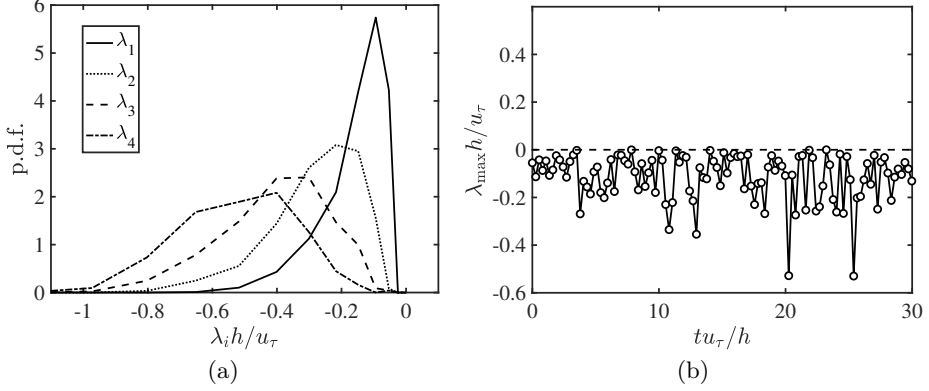


Figure 13: (a) Probability density functions of the growth rate of the four least stable eigenvalues of  $\tilde{\mathcal{L}}(U_0)$ ,  $\lambda_1 > \lambda_2 > \lambda_3 > \lambda_4$ . (b) The history of the most unstable eigenvalue  $\lambda_{\max}$  of  $\tilde{\mathcal{L}}(U_0)$ . Results are for the channel with suppressed modal instabilities NF-SEI180.

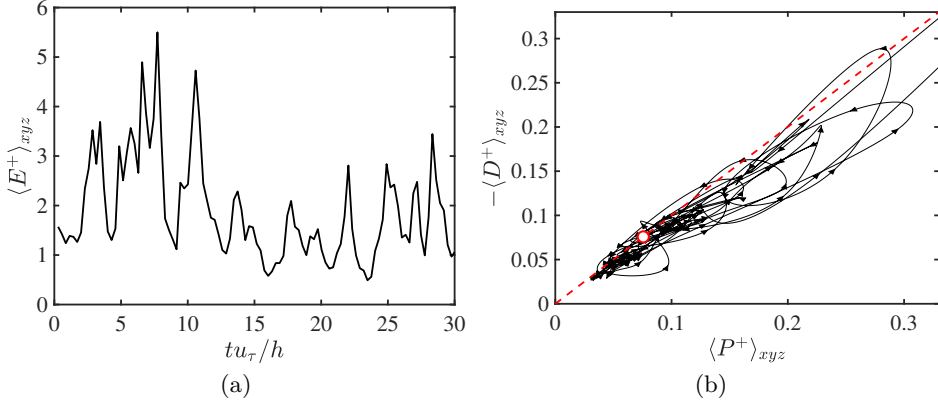


Figure 14: (a) The history of the turbulent kinetic energy  $E = \frac{1}{2} \mathbf{u}' \cdot \mathbf{u}'$  averaged over the channel domain. Note that that only  $30h/u_\tau$  units of time are show in the panel but the simulation was carried out for more than  $300h/u_\tau$ . (b) Projection of the flow trajectory onto the average production rate  $\langle P \rangle_{xyz}$  and dissipation rate  $\langle D \rangle_{xyz}$  plane. The arrows indicate the time direction of the trajectory, which on average rotates counter-clockwise. The red dashed line is  $\langle P \rangle_{xyz} = -\langle D \rangle_{xyz}$  and the red circle  $\langle P \rangle_{xyzt} = -\langle D \rangle_{xyzt}$ . The trajectory projected covers  $30h/u_\tau$  units of time. Results are for the channel with suppressed modal instabilities NF-SEI180.

a segment of the time-series of the maximum modal growth rate of  $\tilde{\mathcal{L}}(U_0)$  are shown in figure 13, which confirms that the system is successfully stabilised.

Figure 14(a) shows the history of the turbulent kinetic energy for NF-SEI180 after initial transients. The result verifies that turbulence persists when  $\mathcal{L}(U_0)$  is replaced by  $\tilde{\mathcal{L}}(U_0)$ . The patterns of the flow trajectories projected onto the production–dissipation plane (figure 14b) also exhibits features similar to those discussed above for R180 and NF180.

The turbulence intensities for NF-SEI180 are presented in figure 15 and compared

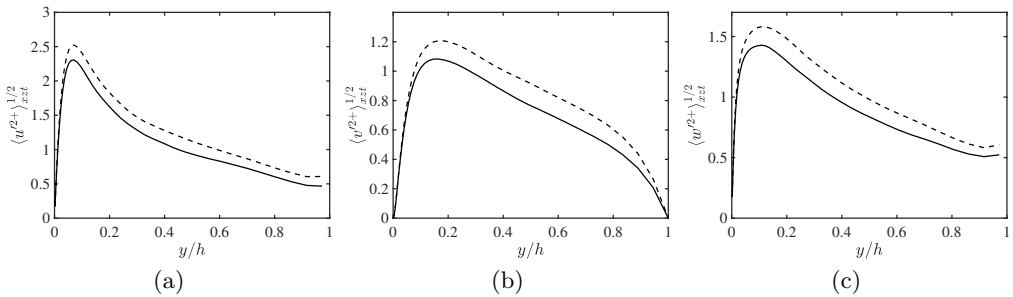


Figure 15: (a) Streamwise, (b) wall-normal, and (c) spanwise root-mean-squared fluctuating velocities as a function of the wall-normal distance for the regular channel R180 (---) and the non-feedback channel with suppressed exponential instabilities NF-SEI180 (—).

with those for NF180. The mean profiles is the same as R180 (not shown). Notably, the channel flow without exponential instabilities is capable of sustaining turbulence. The new flow equilibrates at a state with fluctuations depleted by roughly 10%–20%. The outcome demonstrates that, even if the linear instabilities of the streak manifest in the flow, they are not required for maintaining wall turbulence.

#### 6.1.1. Case with explicit feedback from $\mathbf{u}'$ to $\mathbf{U}$ allowed

It was shown above that turbulence is sustained despite the absence of exponential instabilities. This was demonstrated for NF180, in which the nonlinear feedback from  $\mathbf{u}'$  to  $\mathbf{U}$  was excluded. We have seen in §5 that inhibiting the feedback from  $\mathbf{u}'$  to  $\mathbf{U}$  actually enhances the turbulence intensities with respect to  $u_\tau$ . This may cast doubts on whether the ‘weaker’ fluctuations from R180 can be sustained when modal instabilities are cancelled out. To clarify this point, we resolve a channel with suppressed exponential instabilities in which the feedback from  $\mathbf{u}'$  to  $\mathbf{U}$  is allowed. The equations of motions in that case are:

$$\frac{\partial \mathbf{u}'}{\partial t} = \tilde{\mathcal{L}}(\mathbf{U})\mathbf{u}' + \mathbf{N}(\mathbf{u}'), \quad (6.5a)$$

$$\frac{\partial \mathbf{U}}{\partial t} = -\mathbf{U} \cdot \nabla \mathbf{U} - \langle \mathbf{u}' \cdot \nabla \mathbf{u}' \rangle_x - \frac{1}{\rho} \nabla \langle p \rangle_x + \nu \nabla^2 \mathbf{U} + \mathbf{f}, \quad \nabla \cdot \mathbf{U} = 0. \quad (6.5b)$$

We refer to this case as “regular channel with suppressed exponential instabilities” or R-SEI180. Note that the only difference of (6.5) from the original Navier–Stokes equations (2.1) is the modally stable  $\tilde{\mathcal{L}}$  instead of  $\mathcal{L}$ . The fluctuations  $\mathbf{u}'$  are dynamically coupled to  $\mathbf{u}'$  via the nonlinear term  $\langle \mathbf{u}' \cdot \nabla \mathbf{u}' \rangle_x$  in (6.5b). We initialise simulations of (6.5) from a flow field of R180 after projecting out the unstable and neutral modes.

The history of  $\lambda_{\max}$  for  $\tilde{\mathcal{L}}(\mathbf{U})$ , shown in figure 16(a), confirms that modal instabilities are successfully removed. Figure 16(b) contains the evolution of the turbulent kinetic energy and demonstrates that turbulence persists under the stabilised linear dynamics of (6.5a). The flow trajectories projected onto the production–dissipation plane (figure 16c) also exhibit similar features to those discussed above for R180 and NF-SEI180.

The mean velocity profiles and turbulence intensities for R-SEI180 and R180 are shown in figure 17. The results are consistent with the trends reported in figure 15 for NF-SEI180 and NF180 simulations: turbulence without modal instabilities sustains despite allowing the feedback from  $\mathbf{u}'$  to  $\mathbf{U}$ . As in NF-SEI180, the resulting velocity fluctuations are

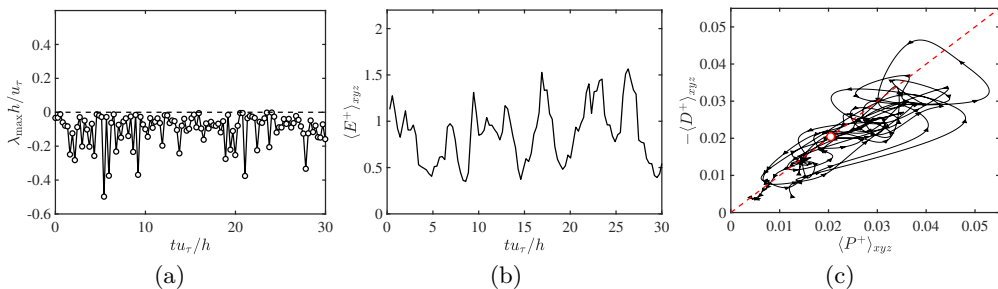


Figure 16: (a) The history of the most unstable eigenvalue  $\lambda_{\max}$  of  $\tilde{\mathcal{L}}(U)$ . Results for channel with suppressed modal instabilities and feedback from  $\mathbf{u}'$  to  $\mathbf{U}$  allowed (R-SEI180). (b) The history of the turbulent kinetic energy of the fluctuation energy  $E = \frac{1}{2}\mathbf{u}' \cdot \mathbf{u}'$  averaged over the channel domain. Note that that only  $30h/u_{\tau}$  units of time are shown in the panels (a) and (b) but the simulation was carried out for more than  $300h/u_{\tau}$ . (c) Projection of the flow trajectory onto the average production rate  $\langle P \rangle_{xyz}$  and dissipation rate  $\langle D \rangle_{xyz}$  plane. The arrows indicate the time direction of the trajectory, which on average rotates counter-clockwise. The red dashed line is  $\langle P \rangle_{xyz} = -\langle D \rangle_{xyz}$  and the red circle  $\langle P \rangle_{xyz} = -\langle D \rangle_{xyz}$ . The trajectory projected covers  $30h/u_{\tau}$  units of time. Results for channel with suppressed modal instabilities but with feedback from  $\mathbf{u}'$  to  $\mathbf{U}$  allowed (R-SEI180).

diminished by roughly 10%. Figure 18 portrays snapshots of the streamwise velocity at three different instants for the R-SEI180 simulation. As in R180 (cf. figure 5), the spatial organisation of the streak cycles through different stages of elongated straight motion, meandering and breakdown, although the first two states (panels (a) and (b)) occur more frequently than in R180. Indeed, if we consider the common definition for the streamwise velocity fluctuation  $u'' = u - \langle u \rangle_{xzt}$ , which contains part of the streak flow, the new flow in R-SEI180 attains an augmented streak intensity as clearly depicted in figure 17(b). The outcome is consistent with the occasional inhibition of the streak meandering or breakdown via exponential instability, which enhances  $u''$ , whereas wall-normal ( $v'' = v'$ ) and spanwise ( $w'' = v'$ ) turbulence intensities are diminished due to a lack of vortices succeeding the collapse of the streak. This behaviour is also observed in many drag reduction investigations (Jung *et al.* 1992; Laadhari *et al.* 1994; Choi & Clayton 2001; Ricco & Quadrio 2008).

As a final comment, it is worth mentioning that in a preliminary work Lozano-Durán *et al.* (2018) showed that turbulence was not sustained when  $\mathcal{L}(U)$  was stabilised by  $\mathcal{L}(U) - \mu \mathcal{I}$ , where  $\mu > 0$  is a damping parameter and  $\mathcal{I}$  is the identity operator. However, it can be shown that introducing the linear drag  $-\mu \mathbf{u}'$  reduces the transient gains supported by  $\mathcal{L}(U)$  by a factor of  $\exp(-2\mu T)$ . Hence, stabilising  $\mathcal{L}(U)$  via a linear drag term  $-\mu \mathbf{u}'$  disrupts the transient growth mechanism severely and this was the cause for the lack of sustained turbulence in Lozano-Durán *et al.* (2018).

## 6.2. Wall turbulence exclusively supported by transient growth

The effect of non-modal transient growth as the main source for energy injection from  $\mathbf{U}$  into  $\mathbf{u}'$  is now assessed by “freezing” the base flow  $U(y, z, t_i)$  at the instant  $t_i$ . In order to steer clear of the potential effect of exponential instabilities, the numerical experiment here is performed using the stabilised linear operator  $\tilde{\mathcal{L}}(U(y, z, t_i))$ . For a given  $U(y, z, t_i)$ , we refer to this case as “channel flow with modally-stable, frozen-in-

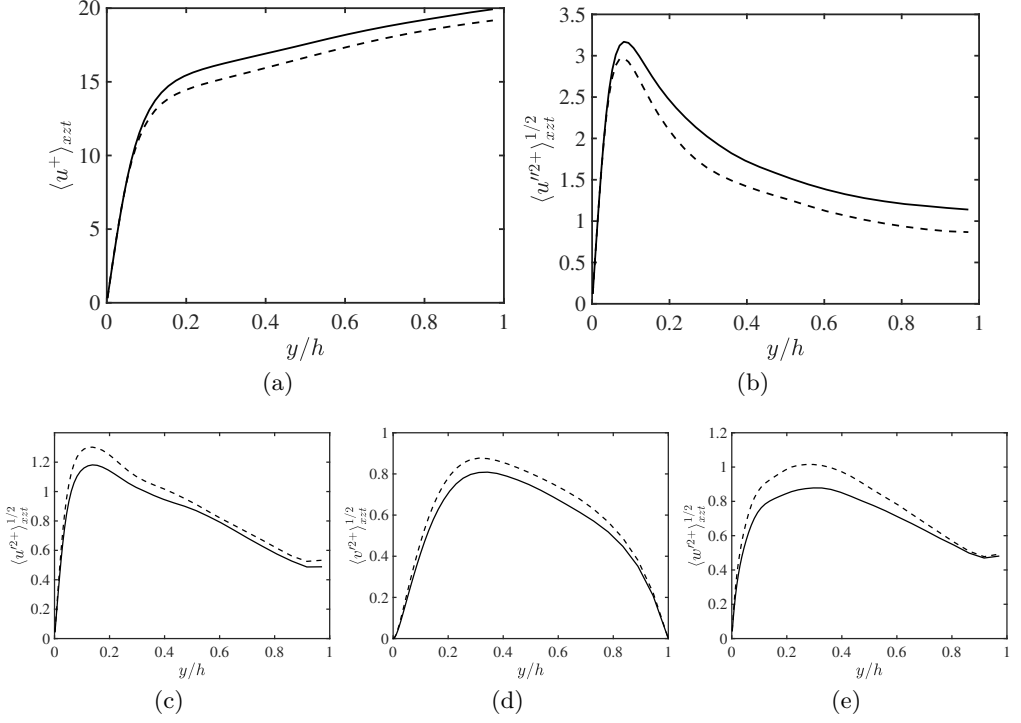


Figure 17: (a) Streamwise mean velocity profile, and (b, c) streamwise, (d) wall-normal, and (e) spanwise mean root-mean-squared fluctuating velocities as a function of the wall-normal distance for the regular channel (R180) (---) and the channel with suppressed exponential instabilities but with the feedback from  $\mathbf{u}'$  to  $\mathbf{U}$  allowed (R-SEI180) (—). Note that the streamwise fluctuating velocity in panel (b) is defined as  $u'' = u - \langle u \rangle_{xzt}$ , while in panel (c) is defined as  $u' = u - U$ .

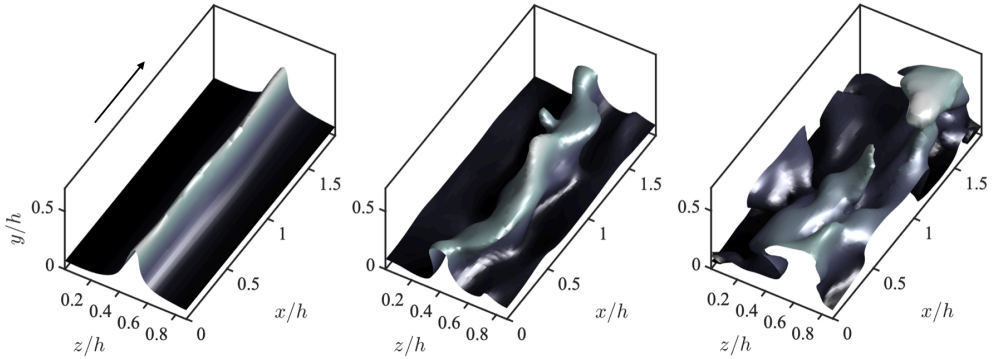


Figure 18: Instantaneous isosurface of the streamwise velocity at different times for R-SEI180. The value of the isosurface is 0.65 of the maximum streamwise velocity. Colours represent the distance to the wall located at  $y = 0$ . The arrow indicates the mean flow direction.



time base-flow”, or NF-TG180<sub>*i*</sub>, with *i* an integer index indicating the case number. Let us denote the flow for NF-TG180<sub>*i*</sub> as  $\mathbf{u}_{\{i\}}$  (and similarly for other flow quantities). The governing equations for NF-TG180<sub>*i*</sub> are

$$\frac{\partial \mathbf{u}'_{\{i\}}}{\partial t} = \tilde{\mathcal{L}}_{\{i\}} \mathbf{u}'_{\{i\}} + \mathbf{N}(\mathbf{u}'_{\{i\}}), \quad (6.6a)$$

$$\mathbf{U}_{\{i\}} = (U(y, z, t_i), 0, 0) \text{ from case R180,} \quad (6.6b)$$

where  $\tilde{\mathcal{L}}_{\{i\}} = \tilde{\mathcal{L}}(U(y, z, t_i))$ . The set-up in (6.6) disposes of energy transfers that are both due to both modal and parametric instabilities, while maintaining the transient growth of fluctuations. For a given  $t_i$ , the simulation is initialised from NF-SEI180 at  $t = t_i$ , and continued for  $t > t_i$ . We performed more than 500 simulations using different frozen base flows  $U(y, z, t_i)$  extracted from R180.

The evolution of the turbulent kinetic energy is shown in figure 19(a) for ten cases NF-TG180<sub>*i*</sub>,  $i = 1, \dots, 10$ . After freezing the base flow at  $t_i$ , most of the cases remain turbulent, while others decay in about  $40h/u_\tau$ . Among all NF-TG180<sub>*i*</sub> simulations, turbulence was sustained in 80% of them. In the cases for which turbulence persists, the projection of the flow trajectory onto the  $\langle P \rangle_{xyz} - \langle D \rangle_{xyz}$  is reminiscent of the self-sustaining cycle for R180; an example is shown in figure 19(b). Since  $\tilde{\mathcal{L}}_{\{i\}}$  is modally stable, a key ingredient to sustain turbulence in NF-TG180<sub>*i*</sub> is the scattering and generation of new disturbances by  $\mathbf{N}(\mathbf{u}'_{\{i\}})$ . Indeed, as we verify in Appendix D, the system (6.6) decays when the nonlinear term  $\mathbf{N}(\mathbf{u}'_{\{i\}})$  is discarded.

The one-point statistics for each NF-TG180<sub>*i*</sub> vary for each  $U(y, z, t_i)$ . To illustrate the differences among cases, figures 19(c,d,e,f) contain the mean velocity profiles and fluctuating velocities for NF-TG180<sub>*i*</sub>,  $i = 1, \dots, 10$ . In some occasions,  $U(y, z, t_i)$  is such that the system equilibrates in a state of intensified turbulence with respect to NF-SEI180, while other base flows result in weakened turbulence. Figure 20 shows instances of the streamwise velocity for representative cases with intensified (top panels) and weakened (bottom panels) turbulent states. The intensified turbulence features a highly disorganised state akin to the a broken streak, whereas the weakened turbulence resembles the quiescent stages of wall turbulence with a well-formed persistent streak.

The intensity and wall-normal behaviour of the turbulence intensities for NF-TG180<sub>*i*</sub> are determined by the fluctuation energy balance

$$\left( \mathbf{u}'_{\{i\}}, (\tilde{\mathcal{L}}_{\{i\}} + \tilde{\mathcal{L}}_{\{i\}}^\dagger) \mathbf{u}'_{\{i\}} \right) + 2 \left( \mathbf{u}'_{\{i\}}, \mathbf{N}(\mathbf{u}'_{\{i\}}) \right) = 0, \quad (6.7)$$

Under the severe assumption that  $\mathbf{N}(\mathbf{u}'_{\{i\}})$  acts as a time-varying forcing whose net effect is independent of  $\mathbf{u}'_{\{i\}}$ , i.e.  $\mathbf{N}(\mathbf{u}'_{\{i\}}) \approx \mathcal{N}_{\{i\}}(t)$  (see, for instance Farrell & Ioannou 1993b; Zare *et al.* 2020), the solution to (6.6a) is obtained via the Green’s function as:

$$\mathbf{u}'_{\{i\}}(t) \approx e^{\tilde{\mathcal{L}}_{\{i\}}(t-t_i)} \mathbf{u}'_{\{i\}}(t_i) + \int_{t_i}^t e^{\tilde{\mathcal{L}}_{\{i\}}(t-\tau)} \mathcal{N}_{\{i\}}(\tau) d\tau, \quad (6.8)$$

The turbulent kinetic energy of (6.8) after transients is

$$\langle E_{\{i\}} \rangle_{xyzt} = \frac{1}{2} \left( \int_{t_i}^t e^{\tilde{\mathcal{L}}_{\{i\}}(t-\tau)} \mathcal{N}_{\{i\}}(\tau) d\tau, \int_{t_i}^t e^{\tilde{\mathcal{L}}_{\{i\}}(t-\tau)} \mathcal{N}_{\{i\}}(\tau) d\tau \right)_t, \quad (6.9)$$

$$= \frac{1}{2} \left( \int_{t_i}^t e^{-\tilde{\mathcal{L}}_{\{i\}}\tau} \mathcal{N}_{\{i\}}(\tau) d\tau, e^{(\tilde{\mathcal{L}}_{\{i\}} + \tilde{\mathcal{L}}_{\{i\}}^\dagger)t} \int_{t_i}^t e^{-\tilde{\mathcal{L}}_{\{i\}}\tau} \mathcal{N}_{\{i\}}(\tau) d\tau \right) \quad (6.10)$$

where in the last equality we took the factors  $e^{\tilde{\mathcal{L}}_{\{i\}}t}$  outside of the integrals and used

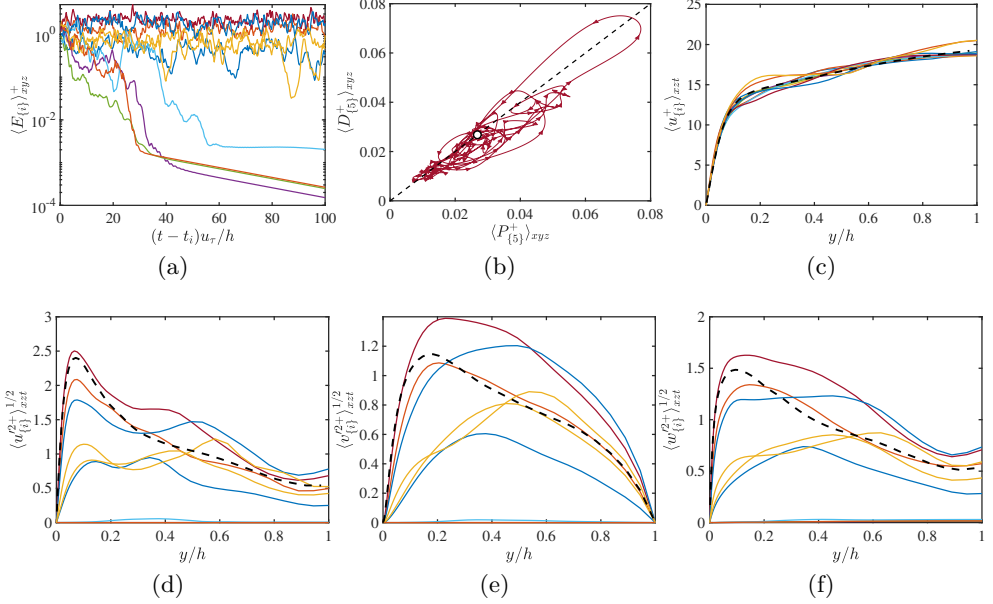


Figure 19: (a) The history of the turbulent kinetic energy of the perturbations  $E_{\{i\}} = \frac{1}{2} \mathbf{u}'_{\{i\}} \cdot \mathbf{u}'_{\{i\}}$  averaged over the channel domain. Different colours denote various case of NF-TG180<sub>i</sub> for  $i = 1, \dots, 10$ . The time  $t_i$  is the instant at which the mean flow is frozen in time. (b) Projection of the flow trajectory onto the average production rate  $\langle P_{\{5\}} \rangle_{xyz}$  and dissipation rate  $\langle D_{\{5\}} \rangle_{xyz}$  plane for NF-TG180<sub>5</sub>. The arrows indicate the time direction of the trajectory, which on average rotates counter-clockwise. The red dashed line is  $\langle P_{\{5\}} \rangle_{xyz} = -\langle D_{\{5\}} \rangle_{xyz}$  and the red circle  $\langle P_{\{5\}} \rangle_{xyz} = -\langle D_{\{5\}} \rangle_{xyz}$ . The trajectory projected covers  $30h/u_\tau$  units of time. (c) Mean velocity profile, and (d) root-mean-squared streamwise, (e) wall-normal, and (f) spanwise fluctuating velocities for ten cases NF-TG180<sub>i</sub>,  $i = 1, \dots, 10$ . The dashed line is for NF-SEI180.

the definition of adjoint operator. After doing a singular-value decomposition on  $e^{\tilde{\mathcal{L}}_{\{i\}} t} = M_{\{i\}} \Sigma_{\{i\}} N_{\{i\}}^\dagger$ ,

$$\langle E_{\{i\}} \rangle_{xyzt} \sim \sigma_{\{i\}, \max}^2 \sim G_{\{i\}, \max}, \quad (6.11)$$

which establishes a link between the level of turbulent kinetic energy and the non-normal energy gain provided by the linear dynamics. The average turbulent kinetic energy of a given case NF-TG180<sub>i</sub> as a function of the maximum gain  $G_{\{i\}, \max}$  at  $T = T_{\max}$  is shown in figure 21(a). The trends suggest that the level of the turbulence intensities at which NF-TG180<sub>i</sub> equilibrates is indeed related to the amount of transient growth supported by  $U(y, z, t_i)$  as anticipated by (6.11). Nonetheless, the scatter of the data in figure 21(a) is still large, which is not surprising as the actual mechanism regulating the intensity of turbulence does not depend exclusively on  $G_{\{i\}, \max}$  but also on the replenishment of fluctuations given by the projection of  $\mathbf{N}(\mathbf{u}'_{\{i\}})$  onto  $e^{\tilde{\mathcal{L}}_{\{i\}} t}$ . Figure 21(a) also suggests that turbulence is not maintained for base flows with  $G_{\{i\}, \max} < 50$ , although this value might be Reynolds number dependent.

To evaluate the compound result of NF-TG180<sub>i</sub>, we define the ensemble average over

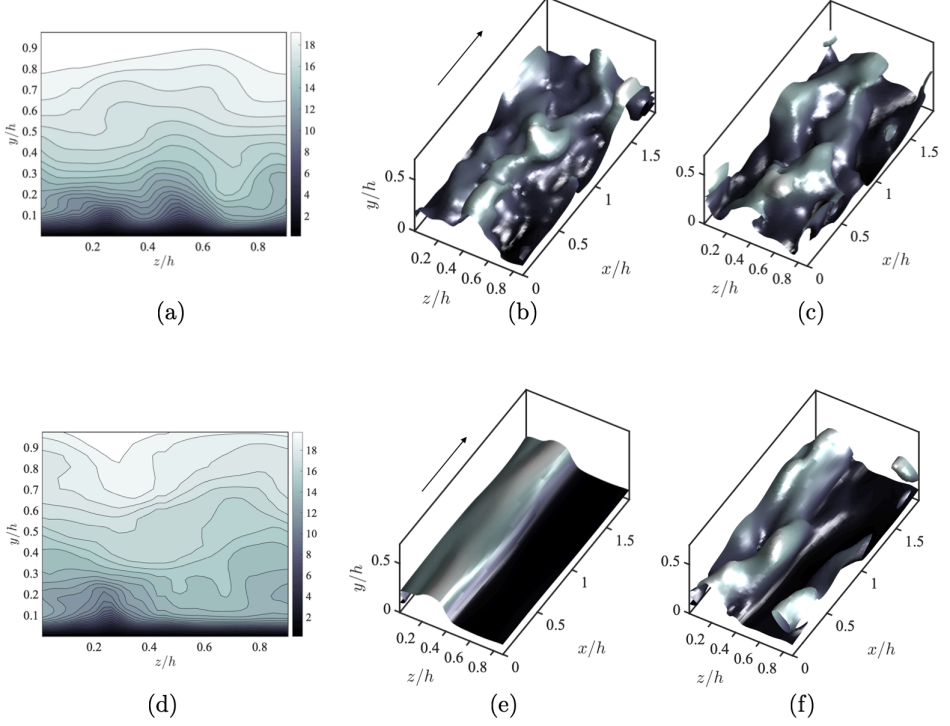


Figure 20: Examples of base flows (a,b) and instantaneous isosurfaces of the streamwise velocity at different times (b,c,e,f). Top panels are for NF-TG180<sub>5</sub>, which is representative of a state with weakened turbulence intensities. Bottom panels are for NF-TG180<sub>10</sub>, which is representative of a state with intensified turbulence. In panels (b,c,e,f), the value of the isosurfaces is 0.65 of the maximum streamwise velocity and colours represent the distance to the wall located at  $y = 0$ . The arrow indicates the mean flow direction.

NF-TG180 <sub>$i$</sub>  of a quantity  $\phi_{\{i\}}$  as

$$\langle \phi_{\{i\}} \rangle_e = \sum_{i=1}^N \frac{\phi_{\{i\}}}{N}, \quad (6.12)$$

where  $1, \dots, N$  is the collection of cases NF-TG180 <sub>$i$</sub>  which remain turbulent. Similarly, the associated standard deviation is defined as  $(\langle \phi_{\{i\}}^2 \rangle_e - \langle \phi_{\{i\}} \rangle_e^2)^{1/2}$ . The ensemble average and standard deviation of the root-mean-squared fluctuating velocities ( $\phi_{\{i\}} = \langle u_{\{i\}}^2 \rangle_{xzt}^{1/2}$ ) is presented in figures 21(b,c,d). The results are compared with those from NF-SEI180, which is similar to NF-TG180 <sub>$i$</sub>  but with time-varying  $U$ . The outcome is striking: the ensemble averages (black solid lines) coincide almost perfectly with the one-point statistics for NF-SEI180 (dashed red lines). Similarly to (6.7), the intensity and wall-normal behaviour of the average turbulent kinetic energy for NF-SEI180 is dictated by the balance

$$\left( \mathbf{u}', (\tilde{\mathcal{L}}(U) + \tilde{\mathcal{L}}^\dagger(U)) \mathbf{u}' \right) + 2 \left( \mathbf{u}', \mathbf{N}(\mathbf{u}') \right) = 0, \quad (6.13)$$

where  $\tilde{\mathcal{L}}(U)$  and  $\mathbf{u}'$  are now the linear operator and velocity vector, respectively, for case NF-SEI180. The excellent agreement between NF-SEI180 and the ensemble average of

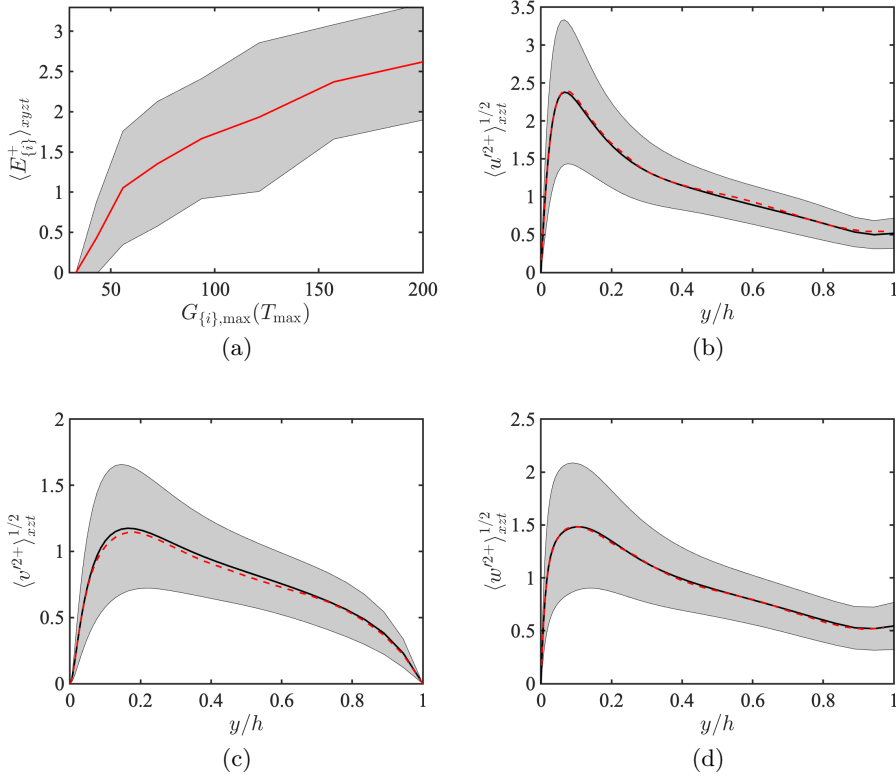


Figure 21: (a) Mean turbulent kinetic energy conditioned to the maximum gain  $G_{\{i\},\max}$  at  $T = T_{\max}$  compiled over NF-TG180 $_i$ ; (—) represents the mean value; the shaded area is  $\pm$  one standard deviation. (b) Root-mean-squared streamwise, (c) wall-normal, and (d) spanwise fluctuating velocities: (—), the ensemble average of all turbulent cases in NF-TG180, namely,  $\langle \langle u_{\{i\}}^2 \rangle_{xzt} \rangle_e$ ,  $\langle \langle v_{\{i\}}^2 \rangle_{xzt} \rangle_e$ , and  $\langle \langle w_{\{i\}}^2 \rangle_{xzt} \rangle_e$ ; the shaded region is  $\pm$  one standard deviation; (---) is  $\langle u^2 \rangle_{xzt}^{1/2}$ ,  $\langle v^2 \rangle_{xzt}^{1/2}$ , and  $\langle w^2 \rangle_{xzt}^{1/2}$  for NF-SEI180.

NF-TG180 $_i$  is remarkable. This agreement suggest that

$$\left( \mathbf{u}'_{\{i\}}, (\tilde{\mathcal{L}}_{\{i\}} + \tilde{\mathcal{L}}_{\{i\}}^\dagger) \mathbf{u}'_{\{i\}} \right)_{te} \approx \left( \mathbf{u}', (\tilde{\mathcal{L}} + \tilde{\mathcal{L}}^\dagger) \mathbf{u}' \right)_t, \quad (6.14)$$

$$\left( \mathbf{u}'_{\{i\}}, \mathbf{N}(\mathbf{u}'_{\{i\}}) \right)_{te} \approx \left( \mathbf{u}', \mathbf{N}(\mathbf{u}') \right)_t. \quad (6.15)$$

An interpretation of figure 21 and of (6.14) is that the collection of linear transient-growth events due to frozen base flows  $U(y, z, t_i)$  at different instances  $t_i$  provides a reasonable representation of the actual time-varying energy transfer from  $\mathbf{U}$  to  $\mathbf{u}'$  in NF-SEI180, at least from the viewpoint of the root-mean-squared fluctuating velocities.

As a final note, in a preliminary work Lozano-Durán et al. (2020) noticed that turbulent channel flows decayed when freezing the base flow, which may initially seem inconsistent with the present results. However, a main difference is that in the present work we are imposing the base flow from actual wall turbulence (R180), while Lozano-Durán et al.

(2020) imposed a base flow from modified turbulence. The statistical sample used here is also larger.

## 7. Conclusions

We have investigated the processes responsible for energy transfers from the streamwise-averaged streaky mean-flow ( $U(y, z, t)$ ) to the turbulent fluctuating flow ( $\mathbf{u}'$ ). This energy transfer is the backbone of the self-sustaining cycle in wall turbulence and a subject of heated debates. The mechanism by which this transfer occurs has long been hypothesised to be correctly captured by the linearized Navier–Stokes equations. Various linear theories stand as tenable candidates to rationalise this process, among them, exponential instabilities of the base flow, neutral modes, non-modal transient growth, and non-modal transient growth supported by parametric instability. To date, a conclusive study regarding the role play by each linear mechanisms has remained elusive due to the lack of clear causal inference provided by traditional non-intrusive tools.

In the present work, we have sensibly modified the Navier–Stokes equations of a turbulent channel flow to preclude one or various linear mechanisms participating in the energy transfer from  $U$  to  $\mathbf{u}'$ . Altering the equations of motion in this manner has the advantage of providing a direct cause-and-effect assessment of the role played by different linear mechanisms in sustaining turbulence. We devised two numerical experiments tailored for minimal turbulent channel units. In the first experiment, the linear operator is modified to render any exponential instabilities of the streaks stable, thus precluding the energy transfer from the mean to the fluctuations via exponential growth. In the second experiment, we simulated turbulent channel flows with prescribed, frozen-in-time, exponentially stable base flows, such that both parametric instabilities as well as exponential instabilities are suppressed.

Our results establish that wall turbulence with realistic mean velocity and turbulence intensities persists even when exponential instabilities are inhibited. While in real flow modal instabilities exist, they are only responsible for only around 10% of the turbulent fluctuating velocities. We have also shown that, for a given frozen-in-time base flow, transient growth alone is capable of sustaining turbulence in the absence of any exponential and parametric instabilities. The resulting turbulence depends of course on the particular base flow selected but, interestingly enough, the ensemble average of multiple cases with different frozen-in-time base-flows reproduces the statistics of realistic turbulences, i.e., those with a time-varying base flow. This last result suggests that the ensemble average of simulations only sustained by transient growth provides a reasonable representation of the actual time-varying energy transfer from  $U$  to  $\mathbf{u}'$ .

Our conclusions here regarding the dynamics of wall turbulence were drawn using direct numerical simulations of the Navier–Stokes equations at low Reynolds numbers representative of the buffer layer. Our analysis was also performed in channels computed using minimal flow units, chosen as simplified representations of naturally occurring wall turbulence. The approach presented in this study paves the way for future investigations at high-Reynolds-numbers turbulence obtained in larger unconstrained domains, in addition to extensions to different flow configurations in which the role of instabilities remains elusive.

A.L.-D. acknowledges the support of the NASA Transformative Aeronautics Concepts Program (Grant No. NNX15AU93A) and the Office of Naval Research (Grant No. N00014-16-S-BA10). N.C.C. was supported by the Australian Research Council (Grant No. CE170100023). This work was also supported by the Coturb project

of the European Research Council (ERC-2014.AdG-669505) during the 2019 Coturb Turbulence Summer Workshop at the Universidad Politécnica de Madrid. M.-A.N. acknowledges the support of the Hellenic Foundation for Research and Innovation, and the General Secretariat for Research and Technology (Grant No. 1718/14518). We thank Jane Bae, Brian Farrell, Petros Ioannou, and Javier Jiménez for insightful discussions. N.C.C. acknowledges his friends for their support during the COVID-19 pandemic.

## Declaration of Interests

The authors report no conflict of interest.

## Appendix A. Details of the stability analysis

This appendix describes the linear stability analysis of a base flow,  $U(y, z, t)$ , which is inhomogeneous in two spatial directions (Karp & Cohen 2014). At given time  $t = t_0$ , we assume the following velocity field

$$\mathbf{u} = (U(y, z, t_0), 0, 0) + \varepsilon \mathbf{u}', \quad 0 < \varepsilon \ll 1, \quad (\text{A } 1)$$

where the base flow  $U$  is assumed parallel, steady, and streamwise independent, and  $\mathbf{u}'$  is the disturbance. Substituting (A 1) into the incompressible Navier–Stokes equations (2.1), neglecting terms of order  $\varepsilon^2$  and higher, and gathering the terms at order  $\varepsilon$ , we obtain the linearized equations for the disturbances:

$$\frac{\partial u'}{\partial x} + \frac{\partial v'}{\partial y} + \frac{\partial w'}{\partial z} = 0, \quad (\text{A } 2a)$$

$$\frac{\partial u'}{\partial t} + U \frac{\partial u'}{\partial x} + v' \frac{\partial U}{\partial y} + w' \frac{\partial U}{\partial z} = -\frac{\partial p'}{\partial x} + \nu \nabla^2 u', \quad (\text{A } 2b)$$

$$\frac{\partial v'}{\partial t} + U \frac{\partial v'}{\partial x} = -\frac{\partial p'}{\partial y} + \nu \nabla^2 v', \quad (\text{A } 2c)$$

$$\frac{\partial w'}{\partial t} + U \frac{\partial w'}{\partial x} = -\frac{\partial p'}{\partial z} + \nu \nabla^2 w'. \quad (\text{A } 2d)$$

The boundary conditions are no slip at the top and impermeability at the wall. Homogeneity in  $x$  and  $t$  allows us to assume that all flow fields for the disturbances take the form, e.g.,

$$u' = \hat{u}'(y, z) e^{(\lambda + i\omega)t + ik_x x}, \quad (\text{A } 3)$$

where  $k_x$  is the streamwise wavenumber, and  $\lambda + i\omega$  is the temporal complex eigenvalue. (Similarly for  $v'$ ,  $w'$ , and  $p'$ .)

Substituting (A 3) into the linearised equations (A 2), they can be rearranged as a generalised eigenvalue problem,

$$\begin{pmatrix} \mathbf{D}_x & \mathbf{D}_y & \mathbf{D}_z & \mathbf{O} \\ \mathbf{C} & \mathbf{U}_y & \mathbf{U}_z & \mathbf{D}_x \\ \mathbf{O} & \mathbf{C} & \mathbf{O} & \mathbf{D}_y \\ \mathbf{O} & \mathbf{O} & \mathbf{C} & \mathbf{D}_z \end{pmatrix} \begin{pmatrix} \tilde{u}' \\ \tilde{v}' \\ \tilde{w}' \\ \tilde{p}' \end{pmatrix} = (\lambda + i\omega) \begin{pmatrix} \mathbf{O} & \mathbf{O} & \mathbf{O} & \mathbf{O} \\ -\mathbf{I} & \mathbf{O} & \mathbf{O} & \mathbf{O} \\ \mathbf{O} & -\mathbf{I} & \mathbf{O} & \mathbf{O} \\ \mathbf{O} & \mathbf{O} & -\mathbf{I} & \mathbf{O} \end{pmatrix} \begin{pmatrix} \tilde{u}' \\ \tilde{v}' \\ \tilde{w}' \\ \tilde{p}' \end{pmatrix}. \quad (\text{A } 4)$$

Here,  $\mathbf{I}$  is the identity matrix,  $\mathbf{O}$  is a zero matrix,  $\tilde{u}'$  is a one-dimensional representation of a two-dimensional vector

$$\tilde{u}' \stackrel{\text{def}}{=} (\hat{u}'(y_1, z_1), \dots, \hat{u}'(y_1, z_{N_z}), \dots, \hat{u}'(y_{N_y}, z_1), \dots, \hat{u}'(y_{N_y}, z_{N_z}))^\top, \quad (\text{A } 5)$$

and similarly for  $\tilde{v}'$ ,  $\tilde{w}'$ , and  $\tilde{p}'$ . Furthermore, the matrices  $\mathbf{C}$ ,  $\mathbf{U}_y$ ,  $\mathbf{U}_z$ ,  $\mathbf{D}_x$ ,  $\mathbf{D}_y$ , and  $\mathbf{D}_z$  are given by

$$\mathbf{C} = ik_x \text{diag}(\mathbf{U}) - \nu (\bar{\mathbf{I}}_z \otimes \bar{\mathbf{D}}_y^2 + \bar{\mathbf{D}}_z^2 \otimes \bar{\mathbf{I}}_y - k_x^2 \bar{\mathbf{I}}_z \otimes \bar{\mathbf{I}}_y), \quad (\text{A } 6a)$$

$$\mathbf{U}_y = \text{diag}\{(\bar{\mathbf{I}}_z \otimes \bar{\mathbf{D}}_y) \mathbf{U}\}, \quad (\text{A } 6b)$$

$$\mathbf{U}_z = \text{diag}\{(\bar{\mathbf{D}}_z \otimes \bar{\mathbf{I}}_y) \mathbf{U}\}, \quad (\text{A } 6c)$$

$$\mathbf{D}_x = ik_x \bar{\mathbf{I}}_z \otimes \bar{\mathbf{I}}_y, \quad (\text{A } 6d)$$

$$\mathbf{D}_y = \bar{\mathbf{I}}_z \otimes \bar{\mathbf{D}}_y, \quad (\text{A } 6e)$$

$$\mathbf{D}_z = \bar{\mathbf{D}}_z \otimes \bar{\mathbf{I}}_y, \quad (\text{A } 6f)$$

where  $\otimes$  is the Kronecker product and  $\mathbf{U}$  is the one-dimensional representation of  $U$  (similarly to  $\tilde{u}'$ ). The matrices  $\bar{\mathbf{I}}_y$  and  $\bar{\mathbf{I}}_z$  are the identity matrices of dimensions  $N_y \times N_y$  and  $N_z \times N_z$ , respectively, and  $\bar{\mathbf{D}}_y$  and  $\bar{\mathbf{D}}_z$  are the matrices that represent differentiation in  $y$  and  $z$  directions, respectively. The eigenvalue problem is solved numerically for all streamwise wavenumbers  $k_x$  on-the-fly during the simulations.

## Appendix B. Validation of eigenvalue calculation

The eigenvalue calculation was numerically implemented in the code which solves the equations of motion such that, at a given time  $t$ , the eigenvalues of  $\mathcal{L}(U(y, z, t))$  are computed on-the-fly. To verify the implementation, a second independent solver was used, which takes as input the base flows  $U(y, z, t)$  stored from the simulation. The second algorithm solves the eigenvalues problem in the vorticity–Laplacian of  $v$  formulation discretised with first-order finite differences in a collocated grid. We have referred to the real part of the eigenvalues computed by the first solver as  $\lambda_j$ . Let us denote the eigenvalues computed by the second solver as  $\check{\lambda}_j$ . Figure 22 shows the history of the real part of the two most unstable eigenvalues  $\lambda_1$  and  $\lambda_2$ , and  $\check{\lambda}_1$  and  $\check{\lambda}_2$ . On average, the error  $|\lambda_j - \check{\lambda}_j|/|\lambda_j|$  for all unstable eigenvalues is of the order of 0.1%. These small differences are somehow expected, as the numerical details of the two solvers differ. Yet, the errors are small enough to provide confidence in the calculation of the modal instabilities. An additional validation is presented in Appendix D.

## Appendix C. Approximate calculation of $\tilde{\mathcal{L}}(U)$ using linear forcing

This appendix presents an alternative approach to suppress exponential instabilities of  $\mathcal{L}(U)$ , which aids the interpretation of the stabilisation of the operator. The approach is also included given its easier implementation using a power methods without the need of the explicit calculation of  $\mathcal{L}(U)$ , which might be beneficial for future works. The eigendecomposition of a normal operator  $\mathcal{A}$  is given by  $\mathcal{A} = Q\Lambda Q^\dagger$ . Operator  $\mathcal{A}$  is stabilised if we subtract its projection to all the eigenspaces that correspond to unstable eigenvalues, i.e., eigenvalues with real part  $\lambda_j > 0$ ,  $j = 1, \dots, N$ :

$$\hat{\mathcal{A}} = \mathcal{A} - \sum_{j=1}^N a \lambda_j \mathbf{u}_j \mathbf{u}_j^\dagger, \quad (\text{A } 1)$$

where  $a$  is a real coefficient  $a > 1$ , and  $\mathbf{u}_j$  is the  $j$ -th eigenmode. The operator  $\mathcal{L}(U)$  is nonnormal and, therefore in its eigendecomposition it is  $Q^{-1}$  that appears and not  $Q^\dagger$ .



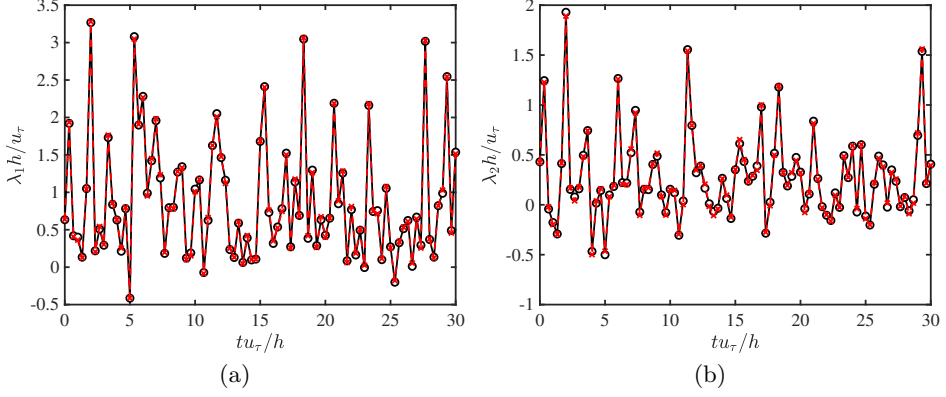


Figure 22: The history of the real part of the two most unstable eigenvalues (a)  $\lambda_1, \check{\lambda}_1$  and (b)  $\lambda_2, \check{\lambda}_2$  of  $\mathcal{L}(U)$  computed on-the-fly by the solver which integrates the equations of motion for the fluctuating velocities ( $- \circ -$ ) and computed *a posteriori* by a second independent solver ( $- \times -$ ).

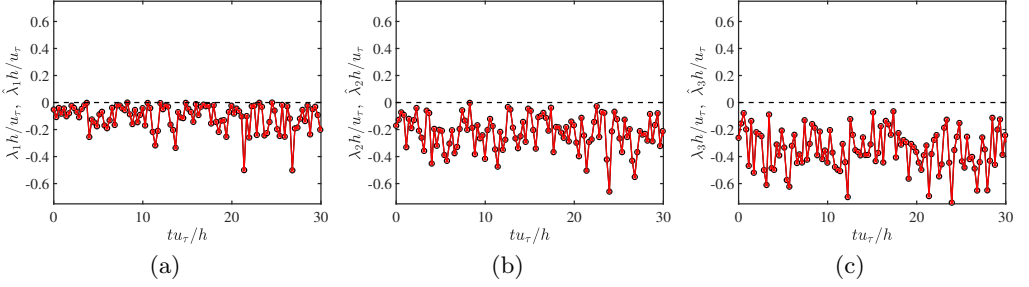


Figure 23: The history of the real part of the three most unstable eigenvalues (a)  $\lambda_1, \hat{\lambda}_1$ , (b)  $\lambda_2, \hat{\lambda}_2$ , (c)  $\lambda_3, \hat{\lambda}_3$  of  $\tilde{\mathcal{L}}(U)$  ( $- \circ -$ ) and  $\hat{\mathcal{L}}(U)$  ( $- \times -$ ).

Thus, an approximation like (A 1), i.e.,

$$\hat{\mathcal{L}}(U) = \mathcal{L}(U) - \sum_{i=1}^N 2\lambda_i \mathbf{u}_i \mathbf{u}_i^\dagger \quad (\text{A } 2)$$

(where we have chosen  $a = 2$ ), is not guaranteed to stabilise  $\mathcal{L}$ . Figure 23 compares the real part of the three most unstable eigenvalues of the properly stabilised  $\tilde{\mathcal{L}}(U)$  (denoted by  $\lambda_i$ ) and those of  $\hat{\mathcal{L}}(U)$  (denoted by  $\hat{\lambda}_i$ ). The approximate method  $\hat{\mathcal{L}}(U)$  succeeds in stabilising  $\mathcal{L}(U)$  with the largest eigenvalues (now stable) obtained within to more than 0.1% accuracy when compared to  $\tilde{\mathcal{L}}(U)$ .

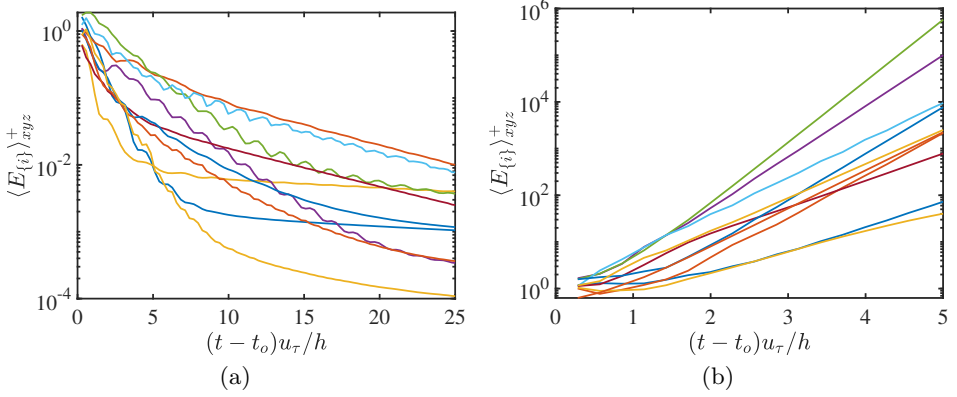


Figure 24: The history of the turbulent kinetic energy of the perturbations  $E = \frac{1}{2} \mathbf{u}' \cdot \mathbf{u}'$  averaged over the channel domain,  $\langle E^+ \rangle_{xyz}$ . Different colours are for cases for (a) modally-stable system (A 1) and (b) modally-unstable system (A 2).  $t_0$  is initial time to integrate the system.

#### Appendix D. Linear analysis of channel flow with a frozen, modally-stable base-flow

We consider the governing equations for the linear channel flow with modally-stable frozen base-flow

$$\frac{\partial \mathbf{u}'}{\partial t} = \tilde{\mathcal{L}}(U) \mathbf{u}', \quad (\text{A } 1a)$$

$$\mathbf{U} = (U(y, z, t_0), 0, 0) \text{ from case R180,} \quad (\text{A } 1b)$$

where we have disposed of the nonlinear term  $\mathbf{N}(\mathbf{u}')$ . We repeat the simulations in §6.2 using the same set-up. As an example, the evolution of the turbulent kinetic energy for ten cases is shown in figure 24(a). Given that  $\tilde{\mathcal{L}}(U)$  is modally stable, the turbulent kinetic energy decays without exception. We verified that this was the case for all the simulations considered in § 6.2 once  $\mathbf{N}(\mathbf{u}')$  is set to zero. Conversely, if we consider the system

$$\frac{\partial \mathbf{u}'}{\partial t} = \mathcal{L}(U) \mathbf{u}', \quad (\text{A } 2a)$$

$$\mathbf{U} = (U(y, z, t_0), 0, 0) \text{ from case R180,} \quad (\text{A } 2b)$$

in which modal instabilities are allowed, the turbulent kinetic energy grows exponentially as seen in figure 24(b) given that the ten cases considered are all such that  $\mathcal{L}(U)$  is modally unstable. It was also verified that the growth rate obtained by integrating (A 2) coincides with the growth rate  $\lambda_1$  of the most unstable mode as predicted by the eigenvalue analysis of  $\mathcal{L}(U)$ . The present appendix serves as validation of the successful suppression of modal instabilities in  $\mathcal{L}(U)$ , and complements the results in figure 13 and the analysis in Appendix B.

## REFERENCES

- ADRIAN, R. J. 2007 Hairpin vortex organization in wall turbulence. *Phys. Fluids* **19** (4), 041301.
- ANDERSSON, P., BRANDT, L., BOTTARO, A. & HENNINGSON, D. S. 2001 On the breakdown of boundary layer streaks. *J. Fluid Mech.* **428**, 29–60.
- BAE, H. J., LOZANO-DURÁN, A., BOSE, S. T. & MOIN, P. 2018 Turbulence intensities in large-eddy simulation of wall-bounded flows. *Phys. Rev. Fluids* **3**, 014610.
- BAE, H. J., LOZANO-DURÁN, A., BOSE, S. T. & MOIN, P. 2019 Dynamic slip wall model for large-eddy simulation. *J. Fluid Mech.* **859**, 400–432.
- BRETHEIM, J. U., MENEVEAU, C. & GAYME, D. F. 2018 A restricted nonlinear large eddy simulation model for high Reynolds number flows. *J. Turb.* **19** (2), 141–166.
- BROWN, GARRY L. & ROSHKO, ANATOL 1974 On density effects and large structure in turbulent mixing layers. *J. Fluid Mech.* **64** (4), 775–816.
- BUTLER, K. M. & FARRELL, B. F. 1993 Optimal perturbations and streak spacing in wall-bounded turbulent shear flow. *Phys. Fluids A* **5**, 774.
- CHERNYSHENKO, S. I. & BAIG, M. F. 2005 The mechanism of streak formation in near-wall turbulence. *J. Fluid Mech.* **544**, 99–131.
- CHINI, G. P., MONTEMURO, B., WHITE, C. M. & KLEWICKI, J. 2017 A self-sustaining process model of inertial layer dynamics in high Reynolds number turbulent wall flows. *Philos. Trans. Royal Soc. A* **375** (2089), 20160090.
- CHOI, K.-S. & CLAYTON, B. R. 2001 The mechanism of turbulent drag reduction with wall oscillation. *Int. J. Heat Fluid Fl.* **22** (1), 1–9.
- CONSTANTINOU, N C, LOZANO-DURÁN, A, NIKOLAIDIS, M-A, FARRELL, B F, IOANNOU, P J & JIMÉNEZ, J 2014 Turbulence in the highly restricted dynamics of a closure at second order: comparison with DNS. *J. Phys.: Conf. Series* **506**, 012004.
- COSSU, C., PUJALS, G. & DEPARDON, S. 2009 Optimal transient growth and very large-scale structures in turbulent boundary layers. *J. Fluid Mech.* **619**, 79–94.
- DEGUCHI, KENGO & HALL, PHILIP 2015 Free-stream coherent structures in growing boundary layers: a link to near-wall streaks. *J. Fluid Mech.* **778**, 451–484.
- DEL ÁLAMO, J. C. & JIMÉNEZ, J. 2006 Linear energy amplification in turbulent channels. *J. Fluid Mech.* **559**, 205–213.
- ELLINGSEN, T. & PALM, E. 1975 Stability of linear flow. *Phys. Fluids* **18** (4), 487–488.
- FARRELL, B. F., GAYME, D. F. & IOANNOU, P. J. 2017 A statistical state dynamics approach to wall turbulence. *Philos. Trans. Royal Soc. A* **375** (2089), 20160081.
- FARRELL, B. F. & IOANNOU, P. J. 1993a Optimal excitation of three-dimensional perturbations in viscous constant shear flow. *Physics of Fluids A: Fluid Dynamics* **5** (6), 1390–1400.
- FARRELL, B. F. & IOANNOU, P. J. 1993b Stochastic forcing of the linearized Navier–Stokes equations. *Phys. Fluids* **5** (11), 2600–2609.
- FARRELL, B. F. & IOANNOU, P. J. 1996a Generalized stability theory. Part I: Autonomous operators. *J. Atmos. Sci.* **53** (14), 2025–2040.
- FARRELL, B. F. & IOANNOU, P. J. 1996b Generalized stability theory. Part II: Non-autonomous operators **53**, 2041–2053.
- FARRELL, B. F. & IOANNOU, P. J. 2012 Dynamics of streamwise rolls and streaks in turbulent wall-bounded shear flow. *J. Fluid Mech.* **708**, 149–196.
- FARRELL, B. F., IOANNOU, P. J., JIMÉNEZ, J., CONSTANTINOU, N. C., LOZANO-DURÁN, A. & NIKOLAIDIS, M.-A. 2016 A statistical state dynamics-based study of the structure and mechanism of large-scale motions in plane Poiseuille flow. *J. Fluid Mech.* **809**, 290–315.
- GIBSON, J. F., HALCROW, J. & CVITANOVTC, P. 2009 Equilibrium and travelling-wave solutions of plane Couette flow. *J. Fluid Mech.* **638**, 243–266.
- DE GIOVANNETTI, M., SUNG, H.J. & HWANG, Y. 2017 Streak instability in turbulent channel flow: the seeding mechanism of large-scale motions. *J. Fluid Mech.* **832**, 483–513.
- HACK, M. J. P. & MOIN, P. 2018 Coherent instability in wall-bounded shear. *J. Fluid Mech.* **844**, 917–955.
- HACK, M. J. P. & ZAKI, T. A. 2014 Streak instabilities in boundary layers beneath free-stream turbulence. *J. Fluid Mech.* **741**, 280–315.
- HALL, P. 2018 Vortex-wave interaction arrays: a sustaining mechanism for the log layer? *J. Fluid Mech.* **850**, 46–82.

- HALL, P. & SMITH, F. T. 1988 The nonlinear interaction of Tollmien–Schlichting waves and Taylor-Görtler vortices in curved channel flows. *Proc. Royal Soc. Lond* **417** (1853), 255–282.
- HALL, P. & SMITH, F. T. 1991 On strongly nonlinear vortex/wave interactions in boundary-layer transition. *J. Fluid Mech.* **227**, 641–666.
- HAMILTON, J. M., KIM, J. & WALEFFE, F. 1995 Regeneration mechanisms of near-wall turbulence structures. *J. Fluid Mech.* **287**, 317–348.
- HÖGBERG, M., BEWLEY, T. R. & HENNINGSON, D. S. 2003 Linear feedback control and estimation of transition in plane channel flow. *J. Fluid Mech.* **481**, 149–175.
- HWANG, Y. & COSSU, C. 2010 Linear non-normal energy amplification of harmonic and stochastic forcing in the turbulent channel flow. *J. Fluid Mech.* **664**, 51–73.
- HWANG, Y. & COSSU, C. 2011 Self-sustained processes in the logarithmic layer of turbulent channel flows. *Phys. Fluids* **23** (6), 061702.
- HWANG, Y., WILLIS, A. P. & COSSU, C. 2016 Invariant solutions of minimal large-scale structures in turbulent channel flow for  $Re_\tau$  up to 1000. *J. Fluid Mech.* **802**, R1.
- JIMÉNEZ, J. 1987 Coherent structures and dynamical systems. *CTR - Proc. Summer Prog.* pp. 323–324.
- JIMÉNEZ, J. 2012 Cascades in wall-bounded turbulence. *Annu. Rev. Fluid Mech.* **44**, 27–45.
- JIMÉNEZ, J. 2013 How linear is wall-bounded turbulence? *Phys. Fluids* **25**, 110814.
- JIMÉNEZ, J. 2018 Coherent structures in wall-bounded turbulence. *J. Fluid Mech.* **842**, P1.
- JIMÉNEZ, J., KAWAHARA, G., SIMENS, M. P., NAGATA, M. & SHIBA, M. 2005 Characterization of near-wall turbulence in terms of equilibrium and “bursting” solutions. *Phys. Fluids* **17** (1), 015105.
- JIMÉNEZ, J. & MOIN, P. 1991 The minimal flow unit in near-wall turbulence. *J. Fluid Mech.* **225**, 213–240.
- JUNG, WJ, MANGIACACCHI, N & AKHAVAN, R 1992 Suppression of turbulence in wall-bounded flows by high-frequency spanwise oscillations. *Physics of Fluids A: Fluid Dynamics* **4** (8), 1605–1607.
- KARP, MICHAEL & COHEN, JACOB 2014 Tracking stages of transition in Couette flow analytically. *J. Fluid Mech.* **748**, 896–931.
- KARP, M. & COHEN, J. 2017 On the secondary instabilities of transient growth in Couette flow. *J. Fluid Mech.* **813**, 528–557.
- KAWAHARA, G., JIMÉNEZ, J., UHLMANN, M. & PINELLI, A. 2003 Linear instability of a corrugated vortex sheet – a model for streak instability. *J. Fluid Mech.* **483**, 315–342.
- KAWAHARA, G. & KIDA, S. 2001 Periodic motion embedded in plane Couette turbulence: regeneration cycle and burst. *J. Fluid Mech.* **449**, 291–300.
- KAWAHARA, G., UHLMANN, M. & VAN VEEN, L. 2012 The significance of simple invariant solutions in turbulent flows. *Annu. Rev. Fluid Mech.* **44** (1), 203–225.
- KIM, J. & BEWLEY, T. R. 2006 A linear systems approach to flow control. *Annu. Rev. Fluid Mech.* **39**, 383–417.
- KIM, J., KLINE, S. J. & REYNOLDS, W. C. 1971 The production of turbulence near a smooth wall in a turbulent boundary layer. *J. Fluid Mech.* **50**, 133–160.
- KIM, JOHN & LIM, JUNWOO 2000 A linear process in wall-bounded turbulent shear flows. *Phys. Fluids* **12** (8), 1885–1888.
- KIM, J. & MOIN, P. 1985 Application of a fractional-step method to incompressible Navier–Stokes equations. *J. Comp. Phys.* **59**, 308–323.
- KLEBANOFF, P. S., TIDSTROM, K. D. & SARGENT, L. M. 1962 The three-dimensional nature of boundary-layer instability. *J. Fluid Mech.* **12** (1), 1–34.
- KLINE, S. J., REYNOLDS, W. C., SCHRAUB, F. A. & RUNSTADLER, P. W. 1967 The structure of turbulent boundary layers. *J. Fluid Mech.* **30** (4), 741–773.
- KREILOS, T. & ECKHARDT, B. 2012 Periodic orbits near onset of chaos in plane Couette flow. *Chaos* **22** (4), 047505.
- LAADHARI, F, SKANDAJI, L & MOREL, R 1994 Turbulence reduction in a boundary layer by a local spanwise oscillating surface. *Phys. Fluids* **6** (10), 3218–3220.
- LANDAHL, M. T. 1975 Wave breakdown and turbulence. *SIAM J. Appl. Math* **28**, 735–756.
- LOZANO-DURÁN, A. & BAE, H.J. 2019 Characteristic scales of Townsend’s wall-attached eddies. *J. Fluid Mech.* **868**, 698–725.

- LOZANO-DURÁN, A., BAE, H.J. & ENCINAR, M.P. 2019 Causality of energy-containing eddies in wall turbulence. *J. Fluid Mech.* **882**, A2.
- LOZANO-DURÁN, A. & BAE, H. J. 2016 Turbulent channel with slip boundaries as a benchmark for subgrid-scale models in LES. *Center for Turbulence Research - Annual Research Briefs* pp. 97–103.
- LOZANO-DURÁN, A. & JIMÉNEZ, J. 2014 Time-resolved evolution of coherent structures in turbulent channels: characterization of eddies and cascades. *J. Fluid. Mech.* **759**, 432–471.
- LOZANO-DURÁN, A., KARP, M. & CONSTANTINOU, N. C. 2018 Wall turbulence with constrained energy extraction from the mean flow. *Center for Turbulence Research - Annual Research Briefs* pp. 209–220.
- LOZANO-DURÁN, A., NIKOLAIDIS, M.-A., CONSTANTINOU, N. C. & KARP, M. 2020 Alternative physics to understand wall turbulence: Navier–Stokes equations with modified linear dynamics. *J. Phys.: Conf. Ser.* **X** (X), in press.
- MCKEON, B. J. 2017 The engine behind (wall) turbulence: perspectives on scale interactions. *J. Fluid Mech.* **817**, P1.
- MCKEON, B. J. & SHARMA, A. S. 2010 A critical-layer framework for turbulent pipe flow. *J. Fluid Mech.* **658**, 336–382.
- MORRA, P., SEMERARO, O., HENNINGSON, D. S. & COSSU, C. 2019 On the relevance of Reynolds stresses in resolvent analyses of turbulent wall-bounded flows. *J. Fluid Mech.* **867**, 969–984.
- NAGATA, M. 1990 Three-dimensional finite-amplitude solutions in plane Couette flow: bifurcation from infinity. *J. Fluid Mech.* **217**, 519–527.
- NIKOLAIDIS, M.-A., FARRELL, B. F., IOANNOU, P. J., GAYME, D. F., LOZANO-DURÁN, A. & JIMÉNEZ, J. 2016 A POD-based analysis of turbulence in the reduced nonlinear dynamics system. *J. Phys.: Conf. Series* **708**, 012002.
- ORLANDI, P. 2000 *Fluid Flow Phenomena: A Numerical Toolkit*. Springer.
- ORR, W. M’F. 1907 The stability or instability of the steady motions of a perfect liquid and of a viscous liquid. Part II: A viscous liquid. *Math. Proc. Royal Ir. Acad.* **27**, 69–138.
- PANTON, R. L. 2001 Overview of the self-sustaining mechanisms of wall turbulence. *Prog. Aerosp. Sci.* **37** (4), 341–383.
- PARK, JAE SUNG & GRAHAM, MICHAEL D. 2015 Exact coherent states and connections to turbulent dynamics in minimal channel flow. *J. Fluid Mech.* **782**, 430–454.
- PEARL, J. 2009 *Causality: Models, Reasoning and Inference*, 2nd edn. New York, NY, USA: Cambridge University Press.
- PUJALS, G., GARCÍA-VILLALBA, M., COSSU, C. & DEPARDON, S. 2009 A note on optimal transient growth in turbulent channel flows. *Phys. Fluids* **21** (1), 015109.
- REDDY, S. C. & HENNINGSON, D. S. 1993 Energy growth in viscous channel flows. *J. Fluid Mech.* **252**, 209–238.
- REYNOLDS, W. C. & HUSSAIN, A. K. M. F. 1972 The mechanics of an organized wave in turbulent shear flow. Part 3. Theoretical models and comparisons with experiments. *J. Fluid Mech.* **54** (2), 263–288.
- RICCO, P. & QUADRIO, M. 2008 Wall-oscillation conditions for drag reduction in turbulent channel flow. *Int. J. Heat Fluid Fl.* **29** (4), 891 – 902.
- SCHMID, P.J. & HENNINGSON, D.S. 2012 *Stability and Transition in Shear Flows*. Springer New York.
- SCHMID, PETER J. 2007 Nonmodal stability theory. *Annu. Rev. Fluid Mech.* **39** (1), 129–162.
- SCHOPPA, W. & HUSSAIN, F. 2002 Coherent structure generation in near-wall turbulence. *J. Fluid Mech.* **453**, 57–108.
- SEKIMOTO, A. & JIMÉNEZ, J. 2017 Vertically localised equilibrium solutions in large-eddy simulations of homogeneous shear flow. *J. Fluid Mech.* **827**, 225–249.
- SMITS, A. J., MCKEON, B. J. & MARUSIC, I. 2011 High-Reynolds number wall turbulence. *Annu. Rev. Fluid Mech.* **43** (1), 353–375.
- TOWNE, A., LOZANO-DURÁN, A. & YANG, X. 2020 Resolvent-based estimation of space–time flow statistics. *J. Fluid Mech.* **883**, A17.
- TOWNSEND, A. A. 1976 *The structure of turbulent shear flow*. Cambridge University Press.

- TREFETHEN, LLOYD N., TREFETHEN, ANNE E., REDDY, SATISH C. & DRISCOLL, TOBIN A. 1993 Hydrodynamic stability without eigenvalues. *Science* **261** (5121), 578–584.
- TUERKE, F. & JIMÉNEZ, J. 2013 Simulations of turbulent channels with prescribed velocity profiles. *J. Fluid Mech.* **723**, 587–603.
- VAN VEEN, L. & KAWAHARA, G. 2011 Homoclinic tangle on the edge of shear turbulence. *Phys. Rev. Lett.* **107**, 114501.
- WALEFFE, F. 1997 On a self-sustaining process in shear flows. *Phys. Fluids* **9** (4), 883–900.
- WALEFFE, F. 2001 Exact coherent structures in channel flow. *J. Fluid Mech.* **435**, 93–102.
- WANG, J., GIBSON, J. & WALEFFE, F. 2007 Lower branch coherent states in shear flows: Transition and control. *Phys. Rev. Lett.* **98**, 204501.
- WEDIN, H. & KERSWELL, R. R. 2004 Exact coherent structures in pipe flow: travelling wave solutions. *J. Fluid Mech.* **508**, 333–371.
- WRAY, A. A. 1990 Minimal-storage time advancement schemes for spectral methods. *Tech. Rep.*. NASA Ames Research Center.
- ZARE, A., GEORGIOU, T. T. & JOVANOVIĆ, M.R. 2020 Stochastic dynamical modeling of turbulent flows. *Annu. Rev. Control Robot. Auton. Syst.* **3** (1), 195–219.
- ZARE, ARMIN, JOVANOVIĆ, MIHAILO R. & GEORGIOU, TRYPHON T. 2017 Colour of turbulence. *J. Fluid Mech.* **812**, 636–680.